



Research papers

Dynamic-wave cellular automata framework for shallow water flow modeling



Tsang-Jung Chang ^{a,b,c}, Hsiang-Lin Yu ^{a,b,*}, Chia-Ho Wang ^{a,c,*}, Albert S. Chen ^d

^a Dept. of Bioenvironmental Systems Engineering., National Taiwan University, Taipei 106, Taiwan

^b Hydrotech Research Institute, National Taiwan University, Taipei 106, Taiwan

^c Center for Weather and Climate Disaster Research, National Taiwan University, Taipei 106, Taiwan

^d Centre for Water Systems, Faculty of Environment, Science and Economy, University of Exeter, Exeter, EX4 4QF, United Kingdom

ARTICLE INFO

This manuscript was handled by A. Bardo, Editor-in-Chief

Keywords:

Shallow water flow
Cellular automata
Dynamic wave
Bernoulli hydraulic head

ABSTRACT

A new dynamic-wave cellular automata framework for two-dimensional (2D) shallow water flow (SWF) modeling is herein proposed. During the last decade, the concept of cellular automata (CA) has been widely adopted to develop various 2D shallow water flow models. Such CA models use simple transition rules that only consider the conservation of mass and neglect the conservation of momentum, as a result, the models behave like the non-inertia wave approximation which are not suitable for modeling strong discontinuous flows (*i.e.*, transcritical flows and wet-dry interfaces). To overcome this limitation, the present study proposes a new CA framework (SWFCA) for 2D shallow water flow modeling, in which the Bernoulli hydraulic head is adopted to replace water level as the key factor to determine water movements. A novel methodology for linking water depths and velocities in the framework is developed. Model verification is carried out through four cases of regular flows and six benchmark cases with strong discontinuous flows. Model efficiency assessment is also conducted to analyze the numerical performance under various flow conditions. The outcomes indicate that the proposed SWFCA model and a non-inertia wave CA-based model (WCA2D) both provide satisfactory results on regular flows. In modeling strong discontinuous flows, the SWFCA model performs better than the WCA2D model and provides the same accuracy as the finite volume model with a HLLC scheme (FV-HLLC). In the aspect of moving wet-dry interfaces and flows under the partially wet condition, the SWFCA model can achieve higher accuracy than the FV-HLLC model. The numerical efficiency of the SWFCA model relates to the flow conditions involved. As the portion of strong discontinuous flows in the computational domain is increasing, the SWFCA model can be up to 305.5% and 121.0%-1282.2% faster than the WCA2D model and the FV-HLLC model, respectively. This novel CA-based framework has been proved its accuracy and efficiency for shallow water flow modeling. Therefore, it has considerable potentials as a useful tool for real-time flood inundation modeling.

1. Introduction

Shallow water flows reflect the conditions in which the water depth is much smaller than the horizontal dimensions of motion (Castro-Orgaz and Hager, 2019). In hydraulic engineering, flows in rivers, floodplains, canals, lakes, reservoirs, and coastal and urban areas are often regarded as shallow water flows and are generally described by the two-dimensional (2D) shallow water equations (SWEs). The 2D SWEs are a set of time-dependent 2D nonlinear partial differential equations of hyperbolic type, which are mathematically the depth-averaged version of the three-dimensional Navier-Stokes equations. In the past two decades, a variety of numerical methods have been used to solve the 2D

SWEs, including mesh-based methods such as finite difference methods, finite element methods, finite volume methods, etc., and meshless methods like smoothed particle hydrodynamics and moving particle semi-implicit. Toro (2001) and Castro-Orgaz and Hager (2019) have extensive summaries on mesh-based methods, and Chang et al. (2014, 2016) and Sarkhosh and Jin (2021) have detailed discussion on meshless methods. So far, the finite volume methods are one of the most commonly-used modeling techniques due to their strong capabilities to efficiently handle flow transition (Xia et al., 2017; Hou et al., 2018; Yu and Chang, 2021; Zhao and Liang, 2022).

Although the aforementioned methods can simulate conditions consisting of transcritical flows and wet-dry interfaces with good

* Corresponding authors at: Dept. of Bioenvironmental Systems Engineering., National Taiwan University, Taipei 106, Taiwan..

E-mail addresses: andy780421@gmail.com (H.-L. Yu), wangchiaho@ntu.edu.tw (C.-H. Wang).

accuracy (Toro, 2001), the numerical efficiency could still be improved, especially for large spatial scale applications. Solving the 2D SWEs at high spatial resolutions demands substantial computational resources, which inevitably increases the required computational time. To enhance numerical efficiency, many researchers established their models using CA framework, such as the CA flood inundation model (Dottori and Todini, 2011), the CA2D model (Ghimire et al., 2013), the flood routing model (Cai et al., 2014), the urban flood inundation model (Liu et al., 2015), the WCA2D model (Guidolin et al., 2016), the OFS-CA model (Jahanbazi et al., 2017), and the CA-ffé model (Jamali et al., 2019), to replace the tedious numerical procedures with a set of simple generic transition rules executed on each computational cell (Wolfram, 1984). In this way, CA framework enables researchers to efficiently simulate complex physics by combining simple algebraic equations without adopting numerical iteration and/or matrix solving (Guidolin et al., 2016). Some of them are coincidentally identical to the finite volume methods under particular choices of numerical schemes (Caviedes-Voullième et al., 2018). Nevertheless, each method has its advantages and drawbacks. The finite volume methods use mathematical approaches (e.g., local Riemann solvers) to explicitly or implicitly solve 2D SWEs, and they often suffer from heavy computational demands. On the other hand, the CA solvers conceptually describe the movement of water by a set of transition rules, thus the efficiency is greatly improved. In particular, the WCA2D model has further lowered its computational demands by incorporating the local weight system, giving significant improvement on efficiency without losing the required accuracy. Thus, it has been widely applied to various applications in conjunction with other models, e.g., water quality (Milašinović et al., 2019; Yin et al., 2020) and urban flood inundation modeling (Wang et al., 2018; Chang et al., 2021). All the aforementioned CA-based models use water levels to determine water movements such that they behave like a non-inertia wave approximation (Caviedes-Voullième et al., 2018). These non-inertia wave models subsequently fail to simulate strong discontinuous flows (i.e., transcritical flows and wet-dry interfaces) but can provide good results on regular flows (hereinafter defined as flows other than strong discontinuous flows) (Costabile et al., 2017). According to the above reviews, numerical models that use explicit CA-based algebraic equations as the transition rules to simulate shallow water flows efficiently and accurately are not yet available.

To fill this gap, the main objective of the study is to develop a new dynamic-wave CA framework for 2D shallow water flow modeling. This new CA-based 2D shallow water flow solver (SWFCA) adopts the Bernoulli hydraulic head instead of water level as the key factor to determine the directions of water movement, and a novel methodology for linking water depths and velocities in the framework is established to sequentially determine the transported amount of mass (water depths) and inertias (water velocities). The SWFCA model is first verified through four cases of regular flows which were previously used to validate the WCA2D model. Then, six benchmark cases with strong discontinuous flows (moving wet-dry interfaces, transcritical flows with hydraulic jump, and dam-break flows) are adopted to compare the accuracy of the SWFCA model, WCA2D model, and a selected finite volume model. Technical attention is given to the local accuracy nearby strong discontinuities. Finally, the numerical efficiency of the SWFCA model in different flow conditions is examined. Detailed discussion is devoted to the numerical performances on the global efficiency of the SWFCA model.

2. Shallow water flow solver based on cellular automata (SWFCA)

In the present study, the SWFCA model that can benefit from the high efficiency of CA framework without losing the required accuracy for simulating both regular flows and strong discontinuous flows is proposed. The SWFCA model adopts the Bernoulli hydraulic head, a new methodology to link the water depths and velocities, instead of the water

level to determine the water movements. To build the SWFCA model on CA framework, three components are required to be processed, i.e., (1) determine the neighborhood configuration, (2) establish variables to describe the state of each discretized computational cell, and (3) evolve the states of computational cells into new time steps by a set of transition rules. These components are introduced in Sections 2.1 to 2.3, respectively. Both the determinations of the adaptive time steps and the assignments of boundary conditions are parts of the transition rules such that they are introduced in Section 2.3. In Section 2.4, the proposed SWFCA and WCA2D models are theoretically compared in the aspects of their numerical accuracy and efficiency.

2.1. Determine the neighborhood configuration

The proposed SWFCA model adopts the square-shaped cell to discretize the studied computational domain for the sake of programming convenience. The SWFCA model selects the Von Neumann neighborhood configuration to define the spatial relation between a central cell and its surrounding cells (Chopard, 2009). Thus, for each central cell, there are four neighbor cells situated at the east, north, west, and south sides. For simplicity, the central cell is indexed as 0, and its neighbor cells at the east, north, west, and south sides are indexed as 1, 2, 3, and 4, respectively, as Fig. 1a depicts. The states of the central cell and its four neighbor cells are all utilized to evolve the states of the central cell into the next time step.

2.2. Establish variables to describe the state of each discretized computational cell

The WCA2D model uses water levels to distribute water directions and relates water velocities with water levels indirectly by utilizing the Manning's and critical flow equations (Guidolin et al., 2016). Hence, the WCA2D model behaves like a non-inertia wave approximation (Chang et al., 2021). To enable the SWFCA model's capacity of handling strong discontinuous flows like dynamic wave models, it is crucial to find an appropriate but simple way to describe the coupled relations between water depths and velocities of 2D SWEs. Thus, the Bernoulli hydraulic head is adopted as an essential factor for this task. Consequently, the states of each computational cell are water depth, water velocity along the x direction, water velocity along the y direction, and the Bernoulli hydraulic head. Other related variables such as bed elevation and Manning's roughness coefficient are both time-invariant variables (i.e., assuming no morphological and roughness changes). All the aforementioned variables are defined at the center of each cell. Herein, the Bernoulli hydraulic head of a central cell is calculated as

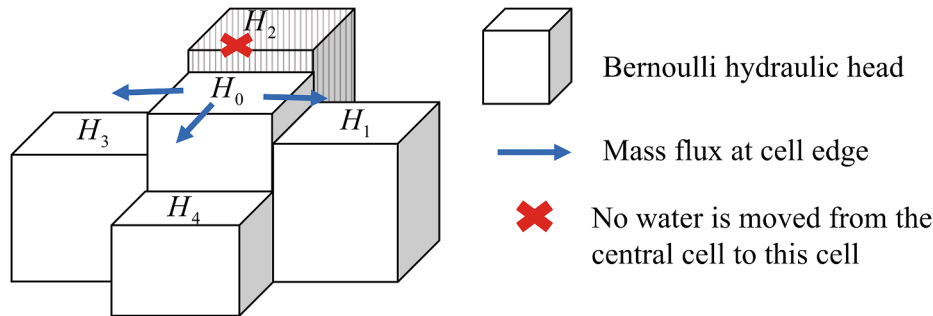
$$H_0 = z_0 + d_0 + \frac{u_0^2 + v_0^2}{2g} \quad (1)$$

where g is the gravitational acceleration ($= 9.81 \text{ m/s}^2$). u_0 and v_0 are the depth-averaged velocities along the x and y directions, respectively, z_0 is the bed elevation, d_0 is the water depth, and H_0 is the Bernoulli hydraulic head of the central cell. In Eq. (1), z_0 , d_0 , $\frac{u_0^2 + v_0^2}{2g}$, and H_0 refer to the elevation head, pressure head, velocity head, and total head, respectively. With the Bernoulli hydraulic head, the SWFCA model gains the ability to simulate flow transition such as hydraulic jump where the consideration of water velocities is essential.

2.3. Evolve the states of computational cells into new time steps by a set of transition rules

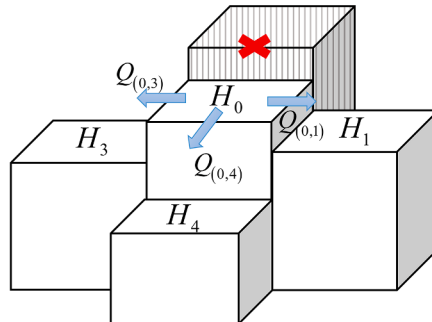
To advance the water depth, water velocities, and Bernoulli hydraulic head at each time step, a computing method comprising a set of transition rules is established to sequentially distribute mass (water depths) and inertias (water velocities) from a central cell to its neighbor cells through four flow transport routes between the central cell and the

- (a) Step 1: Determine the flow direction based on the Bernoulli hydraulic head (H) and mass flux

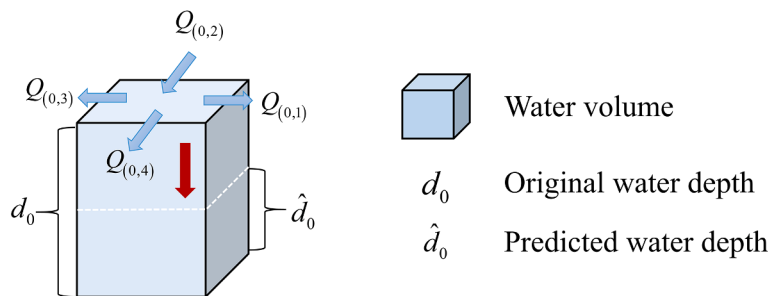


- (b) Step 2: Update the mass flux at each flow transport route in Step 1

$$Q = \min(Q_{Manning}, Q_{Weir})$$



- (c) Step 3: Calculate the predicted water depth of each cell from the mass fluxes in Step 2



* $Q_{(0,2)}$ is from the 2nd neighbor cell

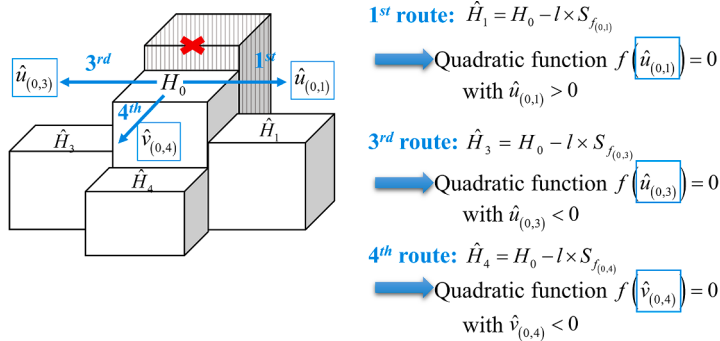
Fig. 1. The schematic illustrations of the five procedures in the computing method under the normal flow condition ($H_0 - H_i \geq \varepsilon$ and $Q_{(0,i)} \times \Theta_{(0,i)} \geq 0$ and $d_0 \geq \delta$) as (a) Step 1, (b) Step 2, (c) Step 3, (d) Step 4, and (e) Step 5.

neighbor cells. For each flow transport route, the Bernoulli hydraulic heads at the centers of the two connected cells and mass flux of the route are used to judge the flow direction of this route for either normal or special flow conditions. The computing method under the normal flow

condition is first introduced in [Section 2.3.1](#). Then, the detection of the special flow condition and the corresponding computing method are introduced in [Section 2.3.2](#). Lastly, [Section 2.3.3](#) presents the calculations of adaptive time steps and assignments of boundary conditions

(d) Step 4: Predict the downstream water velocity at each route based on updated \hat{d}_0 in Step 3

The **Bernoulli principle with friction loss** at each route (by the standard step method)



(e) Step 5: Update the water depth, velocities and Bernoulli hydraulic head of each cell from Steps 3 and 4

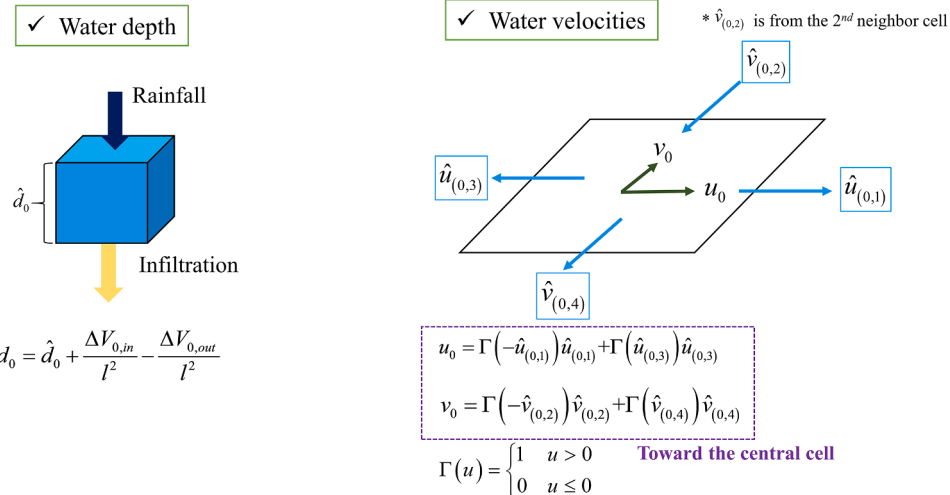


Fig. 1. (continued).

after the water depths and velocities in the computational domain are all updated.

2.3.1. Computing method (normal flow condition)

The computing method under the normal flow condition consists of five sequential steps. They are introduced as follows:

Step 1: Determine the flow direction based on the Bernoulli hydraulic head and mass flux

In this study, the central cell sends out mass and inertias through a flow transport route on the condition that (1) the Bernoulli hydraulic head of the central cell is greater than the neighbor cell, (2) the mass flux of this route is outward from the central cell or zero, and (3) the water depth of the central cell is greater than a threshold. The first and second criteria refer to the flow directions at the next and current time steps, respectively. The second criterion is incorporated to prevent the potential checkerboard instability problem that the flow directions change oppositely between the two subsequent time steps (Bates et al., 2010). The third criterion represents a restriction that no mass and inertias can leave a dry cell. Based on the three criteria, concerning a wet cell, when

the mass flux of a route is zero, the flow direction of the route is decided by criterion one only. On the other hand, if the mass flux is not zero, both criteria 1 and 2 determine the flow direction. Considering the route between the central cell and i^{th} neighbor cell for illustration, the above three criteria are respectively formulated as the three inequalities in Eq. (2)

$$H_0 - H_i \geq \epsilon \text{ and } Q_{(0,i)} \times \Theta_{(0,i)} \geq 0 \text{ and } d_0 \geq \delta \quad (2)$$

where ϵ is the tolerance of the Bernoulli hydraulic head difference, δ refers to the water depth threshold that defines the central cell to be dry or wet, i is the index of the neighbor cell ($i = 1$ to 4), $(0, i)$ represents the i^{th} flow transport route between the central cell and i^{th} neighbor cell, H_0 and H_i are the Bernoulli hydraulic heads at the central cell and i^{th} neighbor cell, respectively, $Q_{(0,i)}$ is the mass flux of this route and is set as zero prior to the simulation, d_0 refers to the water depth of the central cell. $\Theta_{(0,i)}$ is an internal variable of $\Theta_{(0,1)} = 1$, $\Theta_{(0,2)} = 1$, $\Theta_{(0,3)} = -1$, and $\Theta_{(0,4)} = -1$ to represent the flow direction. It is noted that $Q_{(0,i)} \times \Theta_{(0,i)} = 0$ is equivalent to $Q_{(0,i)} = 0$. Taking the central cell in Fig. 1a as an example, there is no flow from the central cell to the 2nd neighbor cell because $H_2 > H_0$. Conversely, the central cell sends out mass and

inertias through the other three routes, and these three routes are marked to be under the *normal flow condition*. The mass and inertia fluxes of the three routes are determined in Steps 2–4.

On the other hand, the flow may move from the wet central cell to the wet neighbor cell despite the Bernoulli hydraulic head of the neighbor cell is greater than the central cell and the mass flux of the route is outward from the central cell. This condition is hereinafter referred to as the *special flow condition* and is resulted from the backwater effect/lateral inflow of the neighbor cell or the lateral outflow from the central cell. To obey the fundamental principle that water flows from larger to smaller Bernoulli hydraulic heads, the magnitude of the mass flux is subsequently lowered (at least to zero) to let the Bernoulli hydraulic head of the central cell greater than that of the neighbor cell. The identification of the special flow condition and the alternative ways for determining flow direction and mass flux are introduced in Section 2.3.2. The inertia flux is computed by using the same step under the normal flow condition (Step 4).

Step 2: Update the mass flux at each flow transport route in Step 1

In Step 2, based on the flow direction decided in Step 1, each central cell updates the mass fluxes of its flow transport routes under the normal flow condition by using the Manning's and weir equations. For the central cell in Fig. 1b, the mass fluxes of its 1st, 3rd, and 4th routes are determined by

$$Q_{(0,i)} = \Theta_i \min(Q_{(0,i),Mann}, Q_{(0,i),Weir}) \quad (3)$$

where $Q_{(0,i),Mann}$ is the mass flux computed by the Manning's equation

$$Q_{(0,i),Mann} = \frac{1}{n_0} l \times \bar{d}_i^{5/3} \sqrt{\frac{(H_0 - H_i)}{l}} \quad (4)$$

in which l is the cell length, n_0 refers to the Manning's roughness coefficient of the central cell, \bar{d}_i is the water depth at the cell edge ($= (d_0 + d_i)/2$). $Q_{(0,i),Weir}$ is the mass flux by the weir equation (Chaudhry, 2022) that is modified to consider the Bernoulli hydraulic head

$$Q_{(0,i),Weir} = \frac{2}{3} l \sqrt{2g} \psi (h_0)^{3/2} \quad (5)$$

$$\psi = \left[1 - (h_i/h_0)^{1.5} \right]^{0.385} \quad (6)$$

in which $\bar{z}_i = \max(z_0, z_i)$, $h_0 = H_0 - \bar{z}_i$, and $h_i = \max(0, H_i - \bar{z}_i)$. In Eq. (6), ψ represents the free (=1) or submerged weir flows. The Manning's and weir equations both relate the Bernoulli hydraulic head to the mass flux, therefore inertias are considered when determining a mass flux.

Step 3: Calculate the predicted water depth of each cell from the mass fluxes in Step 2

After the mass flux of each flow transport route is updated in Step 2, the predicted water depth of each central cell (\hat{d}_0) is then calculated by

$$\hat{d}_0 = d_0 + \frac{\Delta t}{l^2} [-Q_{(0,1)} - Q_{(0,2)} + Q_{(0,3)} + Q_{(0,4)}] \quad (7)$$

in which Δt is the adaptive time step, $Q_{(0,1)}$, $Q_{(0,2)}$, $Q_{(0,3)}$ and $Q_{(0,4)}$ are the computed mass fluxes by Eq. (3) or Eq. (22) of the 1st, 2nd, 3rd, and 4th routes, respectively, as Fig. 1c displays. Eq. (7) is a simple equation that is based on mass conservation. After the predicted water depth of each central cell is computed, the computing method checks if any predicted water depth is negative. Also, the flow directions determined in Step 1 should remain unchanged with these predicted water depths. Taking the 1st route in Fig. 1b as an example, a criterion is applied to check if the flow direction is unchanged

$$H_0 - \varepsilon > z_1 + \hat{d}_1 + \frac{u_1^2 + v_1^2}{2g} \quad (8)$$

If negative predicted water depths are detected and/or Eq. (8) is not satisfied, Δt in Eq. (7) is globally decreased and Step 3 is redone again.

Step 4: Predict the downstream water velocity of each flow transport route based on the predicted water depths in Step 3

In this step, the inertia flux of a flow transport route with a flow through is determined by calculating the predicted water velocity at the downstream end of the route. A specific form of the energy equation with friction loss is used for this task due to its simplicity in relating the water depths and velocities. For the central cell in Fig. 1d, the adopted energy equation of the three routes can be formulated in a general form written in an implicit manner

$$\hat{H}_i = \hat{H}_0 - l \times \hat{S}_{f_{(0,i)}} \quad (9)$$

in which l is the length, \hat{H}_0 and \hat{H}_i are the updated Bernoulli hydraulic heads of the central and i^{th} neighbor cells, respectively, and $\hat{S}_{f_{(0,i)}}$ is the updated friction loss of the i^{th} route. In Eq. (9), all terms except length l are undetermined. The central and the i^{th} neighbor cells are at the upstream and downstream ends of the route, respectively. With Eq. (9), the SWFCA model considers the effects of the convective acceleration, water pressure gradient, bed slope, and friction slope terms in the 2D SWEs from the velocity head, pressure head, and elevation head, and friction loss, respectively. As to the local acceleration of 2D SWEs, it is indirectly simulated in the established transition rules. Nevertheless, Eq. (9) has too many variables to be solved and thus it is explicitly expressed by the standard step method. The only undetermined variable is the water velocity at the downstream end of the route. Taking the 1st route in Fig. 1d as an example, the explicitly expressed Eq. (9) of the route is written as

$$\underbrace{\left\{ \frac{[\hat{u}^2]_{(0,1)} + [v^2]_1}{2g} + \hat{d}_1 + z_1 \right\}}_{\hat{H}_1} = \underbrace{H_0}_{\hat{H}_0} - \underbrace{\frac{l}{2} \left\{ \frac{n_1^2 |u_1| |\hat{u}_{(0,1)}|}{\hat{d}_1^{4/3}} + \frac{n_0^2 u_0^2}{\hat{d}_0^{4/3}} \right\}}_{l \times \hat{S}_{f_{(0,1)}}} \quad (10)$$

in which $\hat{u}_{(0,1)}$ is the predicted water velocity at the downstream (1st neighbor cell) of this route and it is the only undetermined variable. \hat{d}_1 , v_1 , and n_1 are the predicted water depth from Step 3, depth-averaged velocity along the y direction, and the Manning's roughness coefficient, respectively, of the 1st neighbor cell. Other variables related to the central cell (H_0 , d_0 , u_0) are at the current time step. The friction loss of the 1st neighbor cell is written in a semi-implicit manner which can help increase the numerical stability, particularly at wet-dry interfaces (Cea and Bladé, 2015). To meet the flow direction determined in Step 1, $\hat{u}_{(0,1)}$ should be larger than 0 (i.e., $\hat{u}_{(0,1)} > 0$) and Eq. (10) is consequently written as Eq. (12)

$$f(\hat{u}_{(0,1)}) = \left\{ \frac{1}{2g} \right\} [\hat{u}_{(0,1)}]^2 + \left\{ \frac{l}{2} \frac{n_1^2 |u_1|}{\hat{d}_1^{4/3}} \right\} \hat{u}_{(0,1)} + \left\{ \frac{[v^2]_1}{2g} + \hat{d}_1 + z_1 + \frac{l}{2} \frac{n_0^2 u_0^2}{\hat{d}_0^{4/3}} \right\} - H_0 \quad (11)$$

$$f(\hat{u}_{(0,1)}) = 0 \quad (12)$$

The two solutions in Eq. (12) can be easily decided without numerical iterations since $f(\hat{u}_{(0,1)})$ is a quadratic function of $\hat{u}_{(0,1)}$, and only the solution that complies with $\hat{u}_{(0,1)} > 0$ is the final answer. Otherwise, $\hat{u}_{(0,1)}$ is given as 0. Similarly, to calculate the predicted water velocities at the downstream of the 3rd and 4th routes in Fig. 1d ($\hat{u}_{(0,3)}$ and $\hat{v}_{(0,4)}$),

respectively), the corresponding quadratic functions of the two variables are respectively given in Eqs. (13) and (14) with $\hat{u}_{(0,3)} < 0$ and $\hat{v}_{(0,4)} < 0$

$$f(\hat{u}_{(0,3)}) = \left\{ \frac{1}{2g} \right\} [\hat{u}_{(0,3)}]^2 - \left\{ \frac{l}{2} \frac{n_3^2 |u_3|}{\hat{d}_3^{4/3}} \right\} \hat{u}_{(0,3)} + \left\{ \frac{[v^2]_3}{2g} + \hat{d}_3 + z_3 + \frac{l}{2} \frac{n_0^2 u_0^2}{d_0^{4/3}} - H_0 \right\} \quad (13)$$

$$f(\hat{v}_{(0,4)}) = \left\{ \frac{1}{2g} \right\} [\hat{v}_{(0,4)}]^2 - \left\{ \frac{l}{2} \frac{n_4^2 |v_4|}{\hat{d}_4^{4/3}} \right\} \hat{v}_{(0,4)} + \left\{ \frac{[u^2]_4}{2g} + \hat{d}_4 + z_4 + \frac{l}{2} \frac{n_0^2 v_0^2}{d_0^{4/3}} - H_0 \right\} \quad (14)$$

The final solutions of $\hat{u}_{(0,3)}$ and $\hat{v}_{(0,4)}$ are both determined in a similar manner of $\hat{u}_{(0,1)}$. It is stressed that no special treatment of the bed elevation is involved when computing the predicted water velocities because the computations use the bed elevations at the cell centers. Therefore, the proposed SWFCA model can correctly predict the water velocity on a steep plate, which is numerically complicated for some finite volume dynamic wave models (Delestre et al., 2012; Xia et al., 2017; Zhao and Liang, 2022). Nonetheless, as the bed slope gradient is not limited in this formulation, an extremely high value of the predicted water velocity may be computed when there is an abrupt change in terrain, which could significantly decrease the adaptive time steps.

When the free water surface is horizontal and all of the water velocities are zero ($u_0 = 0, v_0 = 0$), i.e., case of water at rest, the Bernoulli hydraulic head of each central cell (Eq. (1)) is exactly the water level ($z_0 + d_0$). In such a condition, each route is judged to have no flow with its mass and inertia fluxes both equal to zero ($Q_{(0,i)} = 0$ in Step 2, and $\hat{u}_{(0,i)} = 0$ or $\hat{v}_{(0,i)} = 0$ in Step 4) such that the SWFCA model can maintain a still free water surface. The above deduction proves that the SWFCA model is inherently able to preserve the well-balanced property (or the C-property) without the need to use a special treatment of bed elevation. On the other hand, for other models such as the finite volume dynamic wave models, a special bed slope discretization that cooperates with the reconstruction method is often required to maintain the well-balanced property (Hou et al., 2013; Cea and Bladé, 2015; Xia et al., 2017; Zhao and Liang, 2022).

Step 5: Update the water depth, velocities, and the Bernoulli hydraulic head of each cell from steps 3 and 4

In this step, the water depth, the water velocities, and the Bernoulli hydraulic head of each central cell are updated. As presented in Fig. 1e, the water depth (d_0) is updated by considering the predicted water depth from Step 3 (\hat{d}_0) and the other input/output water volumes as

$$d_0 = \hat{d}_0 + \frac{\Delta V_{0,in}}{l^2} - \frac{\Delta V_{0,out}}{l^2} \quad (15)$$

in which $\Delta V_{0,in}$ refers to the input water volume of the central cell such as the precipitation and inflows from upstream catchments, $\Delta V_{0,out}$ is the output water volume of the central cell such as the infiltration or lateral outflows. Concerning the update of water velocities (u_0, v_0), the predicted water velocities at the downstream of the routes through which the central cell sends water are considered as

$$u_0 = \Gamma(-\hat{u}_{(0,1)}) \hat{u}_{(0,1)} + \Gamma(\hat{u}_{(0,3)}) \hat{u}_{(0,3)} \quad (16)$$

$$v_0 = \Gamma(-\hat{v}_{(0,2)}) \hat{v}_{(0,2)} + \Gamma(\hat{v}_{(0,4)}) \hat{v}_{(0,4)} \quad (17)$$

with Γ function given as.

$$\Gamma(u) = \begin{cases} 1 & u > 0 \\ 0 & u \leq 0 \end{cases} \quad (18)$$

2.3.2. Computing method (special flow condition)

The special flow condition refers to the condition that the mass flux of a flow transport route is outward from a wet central cell to its wet i^{th} neighbor cell when the central cell has a smaller Bernoulli hydraulic head than the neighbor cell. This condition is the consequence of the backwater effect/lateral inflow at the neighbor cell or the lateral outflow of the central cell. In this flow condition, the flow through the route is damped, leading to two possible circumstances, i.e., (1) the flow direction of the route is unchanged but the magnitudes of the transported mass and inertias are both decreased, or (2) the flow direction is reversed. In the present study, the second circumstance is excluded because the flow direction changes oppositely between the subsequent time steps in this circumstance. To fulfill the basic rule that water can only move from larger to smaller Bernoulli hydraulic heads, alternative ways to delineate the flow direction and determine the mass flux of the route are herein proposed. The same method is used to calculate the predicted water velocity at the downstream end of the route (Step 4 in Section 2.3.1).

First, if a flow transport route does not satisfy Eq. (2), its flow direction is decided by a simple formula in analogy to the normal flow condition (Step 1) as

$$H_i - H_0 \geq \varepsilon \text{ and } Q_{(0,i)} \times \Theta_{(0,i)} > 0 \text{ and } d_0 \geq \delta \text{ and } d_i \geq \delta \quad (19)$$

in which $H_i - H_0 \geq \varepsilon$ violates the aforementioned basic rule and requires adjustment to follow the basic rule. If Eq. (19) is fulfilled, this route is marked to be under the special flow condition. As illustrated in Fig. 2a, the 1st route does not fulfill Eq. (2) but satisfies Eq. (19) such that there is a flow from the central cell through this route. Otherwise, there is no flow.

After the flow direction is determined, the mass flux of this route is computed in an alternative way to let the Bernoulli hydraulic head of the central cell be greater than the neighbor cell again (Step 2). As drawn in Fig. 2b, the magnitude of the mass flux ($Q_{(0,1)}$) at the 1st route is lowered with a magnitude as $\Delta Q_{(0,1)}$ to satisfy Eq. (2), resulting in the inequality as

$$\left(H_0 + \frac{\Delta Q_{(0,1)} \Delta t}{l^2} \right) - \left(H_1 - \frac{\Delta Q_{(0,1)} \Delta t}{l^2} \right) \geq \varepsilon \quad (20)$$

in which $H_0 + \frac{\Delta Q_{(0,1)} \Delta t}{l^2}$ represents the increased Bernoulli hydraulic head of the central cell, $H_1 - \frac{\Delta Q_{(0,1)} \Delta t}{l^2}$ refers to the lowered Bernoulli hydraulic head of the neighbor cell, $\Delta Q_{(0,1)} \frac{\Delta t}{l^2}$ is the change of Bernoulli hydraulic head due to the change of water depth (pressure head). It is noted that the 1st neighbor cell should remain as a wet cell after this adjustment, i.e., $\Delta Q_{(0,1)} \frac{\Delta t}{l^2} \leq d_1 - \delta$. Considering the equal sign in Eq. (20), $\Delta Q_{(0,1)}$ is formulated as

$$\Delta Q_{(0,1)} = \min \left(\frac{l^2}{2 \Delta t} (H_1 - H_0 + \varepsilon), \frac{l^2}{\Delta t} (d_1 - \delta) \right) \quad (21)$$

The computed mass flux ($Q_{(0,1)}$) is finally given as

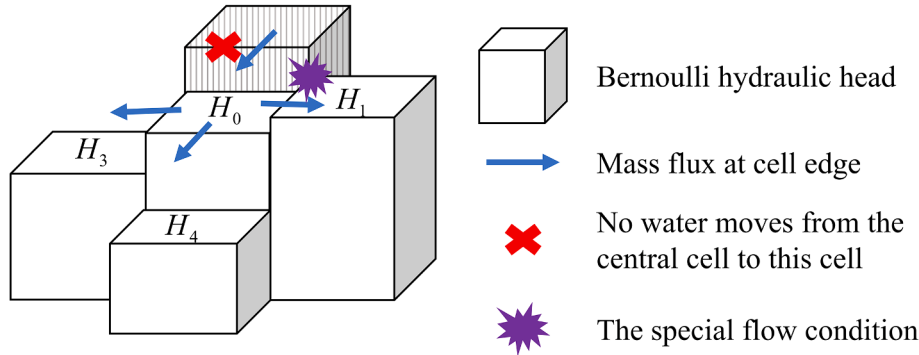
$$Q_{(0,1)} = \text{sign}(Q_{(0,1)}) (|Q_{(0,1)}| - \Delta Q_{(0,1)}) \quad (22)$$

where sign is the sign function. It is noted that if $|Q_{(0,1)}| - \Delta Q_{(0,1)}$ is less than 0, there is no flow through this route, i.e., $Q_{(0,1)} = 0$. For the other routes, the mass fluxes of them can be adjusted in the same way if they are marked to be under the special flow condition.

2.3.3. Stability criterion and boundary conditions

2.3.3.1. Stability criterion. The SWFCA model follows the Courant-

(a) Detection of the special flow condition in Step 1



(b) Determine the mass flux of the flow transport route under the special flow condition in Step 2

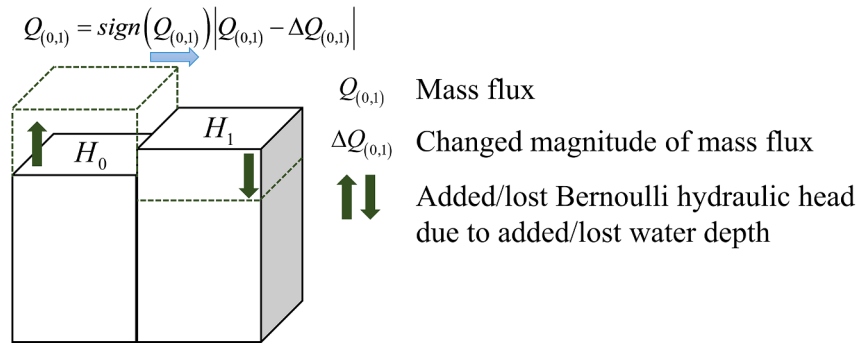


Fig. 2. The illustration of the special flow condition in the proposed computing method ($H_i - H_0 \geq \varepsilon$ and $Q_{(0,i)} \times \Theta_{(0,i)} > 0$ and $d_0 \geq \delta$ and $d_i \geq \delta$). (a) The detection of the special flow condition (Step 1) and (b) the treatment to calculate the mass flux of a flow transport route under the special flow condition (Step 2). The calculation of the predicted water velocity is the same as Step 4 in the normal flow condition.

Friedrichs-Lowy (CFL) condition to determine the adaptive time step

$$\Delta t = \text{CFL} \min \left(\frac{l}{\sqrt{u^2 + v^2} + \sqrt{gd}} \right) \quad (23)$$

where CFL is the Courant number that ranges between 0 and 1.

2.3.3.2. Boundary conditions. In the SWFCA model, the assignments of boundary conditions are processed after Step 5. Closed, inlet and outlet boundaries are considered herein. No mass and inertias can pass through a closed boundary (the same as a reflective boundary), thus there is no input/output water volume at the adjacent computational cell and the water velocity of the cell is unchanged. At an inlet boundary, the water depth of the inner computational cell is updated by adding the inflow (m^3/s) as an input water volume. To consider the inertia effect of the inflow, the water velocity of the inflow is determined according to the specified flow condition. Under supercritical flows, this water velocity (u or v) is imposed by the user. In cases of subcritical flows, the water velocity is calculated by using the water depth at the cell as $\frac{Q}{l \times d_0}$. For critical flows, the critical water depth (d_{critical}) of the given mass flux Q is first calculated by the critical flow equation

$$d_{\text{critical}} = \left(\frac{Q}{l^2 \times g} \right)^{1/3} \quad (24)$$

Then the water velocity of the inflow is computed ($= \frac{Q}{l \times d_{\text{critical}}}$) and the water velocity of the cell along the normal direction of the inflow is

subsequently updated. Next, the Bernoulli hydraulic head of the cell is calculated again (Eq. (1)). At an outlet boundary, the outflow (m^3/s) is determined by using the water depth and velocity of the inner computational cell according to the alignment of the outlet boundary ($Q = l \times u_0 \times d_0$ or $Q = l \times v_0 \times d_0$), and the water depth of the cell is subsequently updated by subtracting the outflow as an output water volume. Then, the water velocity of the outflow is computed to include the inertia effect of the outflow. For supercritical flows, the water velocity is calculated by using the water depth of the inner computational cell. As to subcritical flows, the water depth imposed by the user is used for computing the water velocity. In terms of critical flows, the critical water depth is determined by Eq. (24) and then the water velocity of the outflow is decided. Next, the water velocity with a direction from the cell to the outlet boundary is used to replace the water velocity of the inner computational cell along the direction normal to the outlet boundary. Finally, the Bernoulli hydraulic head of the cell is calculated again.

2.4. Comparison of the computing method and solving procedures between the WCA2D and SWFCA models

The major difference between the WCA2D and SWFCA models is on the computation of water movement between adjacent cells. The WCA2D model uses water levels to determine the intercellular-volumes of water across cell edges. As it lacks the inertia terms, the permissible intercellular velocities involved in the computations are subsequently determined based on water level gradients by using the Manning's and

critical flow equations (Guidolin et al., 2016). The magnitude and direction of an intercellular-volume may change rapidly between subsequent time steps. Hence, the WCA2D model can only handle critical and subcritical flows because the intercellular velocities are constrained by the critical flow equation (Guidolin et al., 2016; Chang et al., 2021) such that the WCA2D model can only obtain accurate results on regular flows under critical/subcritical flow conditions. On the other side, the proposed SWFCA model uses the Bernoulli hydraulic head to distribute water such that the spatial and temporal changes of inertias are both simulated. The computing method of the SWFCA model uses the Bernoulli hydraulic head and a particular form of the energy equation with friction loss to decide the changes in mass and inertias through flow transport routes. As the adopted energy equation is a special form of the 2D SWEs, the SWFCA model is expected to accurately handle regular flows and strong discontinuous flows like the dynamic wave models. The accuracy of the two CA-based models is next compared in Section 3.

As to the numerical efficiency, the execution time on CPU instead of GPU is used for comparison since the technique of parallelization is beyond the scope of this manuscript. The total CPU time is influenced by two factors, i.e., the required time to execute the solving procedure in each time step and the magnitudes of adaptive time steps. In terms of the solving procedures in each time step, the WCA2D model consists of two steps to determine the intercellular-volumes and update the state of each central cell based on these intercellular-volumes (Guidolin et al., 2016). The SWFCA model comprises four steps (Steps 1 to 4 in Section 2.3.1) to determine the fluxes of mass and inertias through each flow transport route and update the states (water depth and velocities) of each central cell based on these fluxes (Step 5 in Section 2.3.1). Hence, the SWFCA model demands more computational effort to execute the solving procedure in each time step compared to the WCA2D model. As to the magnitudes of adaptive time steps, the WCA2D model behaves like the non-inertia wave approximation, thus it takes the minimum value between the CFL condition and the formula given by Hunter et al. (2005) as the adaptive time step to maintain its numerical and physical stabilities. On the other side, as the SWFCA model simulates inertias like the other dynamic wave models, the adaptive time step of it is calculated by the CFL condition only. The relative relationship between the WCA2D and SWFCA models in terms of the adaptive time steps is thus similar to that of the non-inertia wave and dynamic wave models, and the WCA2D model is expected to use smaller adaptive time steps than the SWFCA model (Hunter et al., 2005; Caviedes-Voullième et al., 2020).

In general, despite the SWFCA model involves more computational procedures within a time step, the total CPU time of these two models is still affected by the magnitudes of the adaptive time steps. Thus, which model is faster is case by case. For a simulation, in milder flow conditions with relatively smooth profiles of water depths and velocities, both the WCA2D and SWFCA models have relatively larger adaptive time steps. By contrast, in severe flow conditions, the adaptive time steps of the WCA2D model are smaller than those of the SWFCA model. Therefore, the SWFCA model could perform faster. Conversely, when the flow conditions in a simulation are largely milder, the efficiency of the WCA2D model can outperform the SWFCA model. Based on the above deduction, the numerical efficiency of the SWFCA model is related to the flow conditions involved. To confirm the above deduction, the numerical efficiency assessment in Sections 4 and 5 is given to compare the efficiency of the proposed SWFCA model with the WCA2D model on the test cases with various flow conditions.

3. Model verification

In this section, the accuracy of the SWFCA model is verified through four cases with regular flows and six benchmark cases of strong discontinuous flows. The widely-used WCA2D model is selected to compare with the SWFCA model. In Section 3.1, the SWFCA model is verified through four regular flow cases, which were previously studied by Guidolin et al. (2016) to demonstrate their WCA2D model. In

subsections 3.2, six benchmark cases with a relatively large portion of strong discontinuous flows are adopted to understand the capability of the proposed SWFCA model on handling this kind of extreme flow conditions. In addition, among various dynamic wave models, the present study chooses the first-order Godunov-type finite volume model to further find out how accurate the proposed SWFCA model can be on simulating strong discontinuous flows. This finite volume model uses the HLLC scheme, which is popularly used in many academic and commercial programs, to compute numerical fluxes on cell edges (Yu and Chang, 2021), and it is hereinafter to be referred to as the FV-HLLC model for simplicity. In these ten cases, the numerical accuracy of each selected model is quantified by calculating the L_2 norm between the numerical and measured/analytical results (Chang et al., 2016; Yu and Chang, 2021).

3.1. Regular flows

Among the cases given by Guidolin et al. (2016), this study selects the first four cases (one 1D analytical case and three EA benchmark cases) for model verification. The first case refers to non-breaking wave propagation over a horizontal plane. In this case, most of the shallow water flows are having low Froude numbers. The other three selected cases are all EA benchmark test cases, including filling of a floodplain (EAT2), flood propagation over an extended floodplain (EAT4), and runoff produced by rainfalls and a point source in an urban area (EAT8a). The grid resolution is 1 m for the first case. Thus, there are 5,001 computational cells in the first case. As to the other three cases, the grid resolutions are 20 m, 5 m, and 2 m, respectively. Hence, the three EA cases have 10,000, 80,000, and 97,000 computational cells, respectively. The rest settings of the four cases are all the same as in Guidolin et al. (2016). To compute L_2 norms for water depths in the four cases, the analytical solution and simulated results reported in Guidolin et al. (2016) are used. In the first case, the simulated/analytical water depth profiles when the time is 3600 s are used for computing L_2 norms. So, there is 5,001 data for each L_2 norm computation. As for the other three cases, the temporal water depth profiles at the specified locations of the selected dynamic wave model in Guidolin et al. (2016) are taken to compute a single L_2 norm for each case. Thus, based on the output frequencies given by Néelz and Pender (2013), the rest three cases respectively use 577, 901, and 601 data to compute their L_2 norms. For the WCA2D model, the L_2 norms are computed by using the simulated results under the fine type slope tolerance which has better accuracy than the coarse type slope tolerance (Guidolin et al., 2016). The values of the fine type slope tolerance can be found in Table 2 of Guidolin et al. (2016).

The calculated L_2 norms for water depths of the WCA2D and SWFCA models in the four cases are listed in Table 1. From Table 1, the L_2 norms of the WCA2D model in these cases are 0.011, 0.003, 0.006, and <0.001 , respectively, and the L_2 norms of the SWFCA model are 0.011, <0.001 , <0.001 , and <0.001 , respectively. The results show that both the WCA2D and SWFCA models simulate regular flows in these four cases accurately. Nevertheless, the accuracy of the SWFCA model is slightly better than the WCA2D model because there are still some strong discontinuous flows in these cases.

Table 1
The numerical accuracy of the WCA2D and SWFCA models on regular flows.

Cases	WCA2D L_2	SWFCA L_2
^a Non-breaking wave propagation over a horizontal plane	0.011	0.011
Filling of floodplain depressions (EAT2)	0.003	<0.001
Flood propagation over an extended floodplain (EAT4)	0.006	<0.001
Runoff caused by rainfall and a point source in a small urban area (EAT8a)	<0.001	<0.001

^a The analytical solution is utilized to calculate the L_2 norm.

3.2. Strong discontinuous flows

Six benchmark cases with a large portion of strong discontinuous flows in the computational domain are adopted herein to verify the accuracy of the proposed SWFCA model. The WCA2D and FV-HLLC models are also selected for comparison. In the first two cases (Cases A and B), unsteady flows with a large portion of moving wet-dry interfaces on uneven terrain are considered. A special focus is devoted to examining the capability of the SWFCA model in simulating moving wet-dry interfaces with changes in terrain (Case A) and very shallow overland flows on the steep hillside (Case B). Then, transcritical flows with a hydraulic jump in the steady state are considered (Case C) to test if the SWFCA model can correctly simulate hydraulic jumps. Then, the SWFCA model is evaluated through three dam-break flow cases on idealized (Case D) and realistic terrain (Cases E and F) to verify its numerical performance on more complicated flow conditions. Case D considers dam-break flows over a symmetric triangular bump with various downstream boundary conditions. In this case, hydraulic jumps/drops, moving wet-dry interfaces, and partially reflective waves occurred. For Case E, a real dam-break event, i.e., the Malpasset dam-break event, is used to test the applicability of the SWFCA model in handling dam-break flows on a realistic terrain with complex river-floodplain interactions. As

the dam-break flows pass through the meander Reyran river valley, strong discontinuous flows (moving wet-dry interfaces, hydraulic jumps/drops) all occur. Finally, in Case F, the present study considers 2D dam-break flows over the field-scale floodplain with a staggered configuration of buildings. When the dam-break flows pass through these buildings, hydraulic jumps occurred in fronts of buildings because of the limited flow paths. Consequently, moving wet-dry interfaces along with the dam-break flows, and hydraulic jumps/drops around the buildings emerged along both x and y directions.

3.2.1. Case A: Moving shorelines in a 2D frictional parabolic bowl (moving wet-dry interfaces)

Case A involves moving shorelines in a 2D frictional parabolic bowl. The analytical bed elevation, water levels, and water velocities are presented by Sampson et al. (2006). Following the works by Hou et al. (2013) and Zhao and Liang (2022), the center of the $8000 \text{ m} \times 8000 \text{ m}$ square computational domain is at (4000 m, 4000 m). As for other parameters, $h_0 = 10 \text{ m}$, $a = 3000 \text{ m}$, $B = 5 \text{ m/s}$ and $\tau = 0.002 \text{ 1/s}$, which leads to $p = 0.0093 \text{ 1/s}$ and $s = 0.0046 \text{ 1/s}$. All boundaries are closed. The bowl-shaped terrain of the computational domain is depicted in Fig. 3a as the topography line for illustration.

Initially, the water levels and velocities of the computational domain

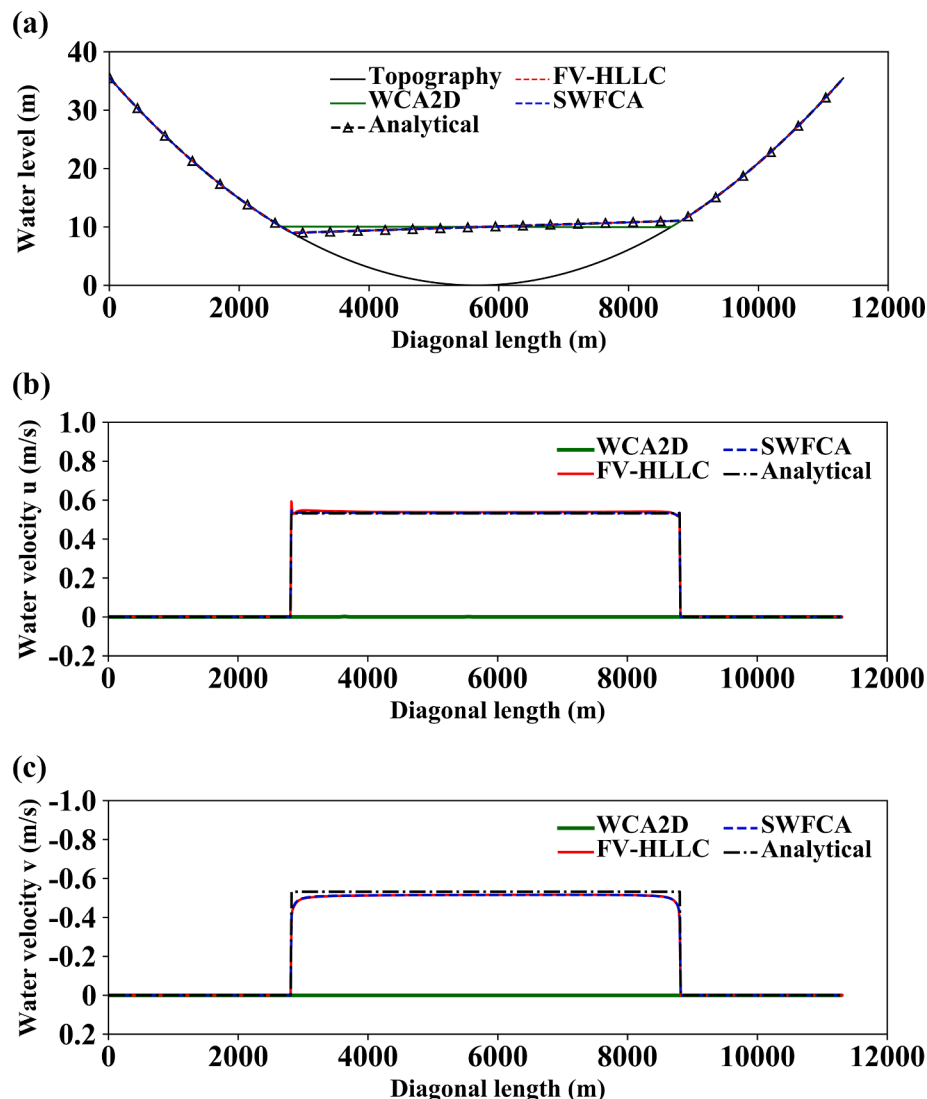


Fig. 3. Moving shorelines in a 2D frictional parabolic bowl (Case A). The comparison between the numerical and analytical profiles on the diagonal line for the (a) water level, (b) u -velocity, and (c) v -velocity at $t = 1.375 T$ s (period $T = 1377.68$ s).

are filled with the analytical values with $t = 0$ s. The simulation duration is 6000 s. As to the setting of friction, the friction parameter τ is used instead of the Manning's roughness coefficient n . Hence, each selected model is modified to use the friction parameter τ . For the FV-HLLC model, the friction slope vector in Eq. (13) of Yu and Chang (2021) is redefined as

$$\mathbf{S}_{f(ij)}^{s+1} = \begin{bmatrix} 0 & -(\tau q_x^{s+1})_{(i,j)} & -(\tau q_y^{s+1})_{(i,j)} \end{bmatrix}^T \quad (25)$$

in which S_f^{s+1} , q_x^{s+1} and q_y^{s+1} are defined in Yu and Chang (2021). Concerning the proposed SWFCA model, Eq. (11) is rewritten as

$$f(\hat{u}_{(0,1)}) = \left\{ \frac{1}{2g} \right\} [\hat{u}_{(0,1)}]^2 + \left\{ \frac{l \times \tau}{2g} \right\} \hat{u}_{(0,1)} + \left\{ \frac{[v^2]_1}{2g} + \hat{d}_1 + z_1 + \frac{l \times \tau}{2g} |u_0| - H_0 \right\} \quad (26)$$

Eqs. (13) and (14) can also be rewritten in the same way. As to the WCA2D model, the maximum permissible intercellular velocity v_M in Eq. (9) and the adaptive time step Δt in Eq. (18) of Guidolin et al. (2016) are respectively rewritten as

$$v_M = \min \left\{ \sqrt{d_0 g}, \frac{g}{\tau} \frac{\Delta l_{0,M}}{\Delta x_{0,M}} \right\} \quad (27)$$

$$\Delta t = \frac{\Delta x^2}{4} \min \left(\frac{\tau}{gR}, S > \sigma \right) \quad (28)$$

The definitions of $\Delta l_{0,M}$, $\Delta x_{0,M}$, R , S and σ can be found in Guidolin et al. (2016). To quantify the accuracy of the selected model, the simulated water level and velocity profiles on the diagonal line between point (0 m, 0 m) and point (8000 m, 8000 m) at $t = 1.375$ T s (period $T = 1377.68$ s) are used to calculate the L_2 norms for water levels and velocities, respectively. A grid convergence test is undertaken first to decide an optimal grid resolution that can lead to an acceptable accuracy. Meanwhile, the numerical diffusion and dispersion properties of the SWFCA model are also investigated. Then, an accuracy comparison among the selected models is performed under this grid resolution.

1. Grid convergence test

Several grid resolutions are considered in this test. For the sake of demonstration, only the results at the grid resolutions of 5 m, 10 m, 25 m, and 50 m are presented here. Consequently, calculations of the L_2 norm at these four grid resolutions take 1,600, 800, 320, and 160 data, respectively. The calculated L_2 norms for water levels and velocities are all listed in Table 2. When the grid resolution becomes finer, all the three L_2 norms are decreased. Furthermore, when the grid resolution is finer than 10 m, the SWFCA model can provide accurate results compared to the analytical solutions, proving the correctness of the SWFCA model on handling the fluxes (mass and inertias), bed elevation, and friction under proper grid resolutions. This result also confirms that the numerical diffusion and dispersion of the SWFCA model become less when the grid resolution is getting finer. Finally, for the accuracy comparison, the grid

Table 2

The L_2 norms for water levels and velocities on the diagonal line at $t = 1.375$ T s ($T = 1377.68$ s) under the four grid resolutions for the grid convergence test of Case A.

Grid resolution (m)	L_2 norm for water levels	L_2 norm for water velocities u	L_2 norm for water velocities v
50	0.002	0.162	0.253
25	0.001	0.068	0.106
10	<0.001	0.005	0.045
5	<0.001	0.003	0.024

resolution of 10 m is selected since the subsequent accuracy is acceptable.

2. Accuracy comparison

The accuracy comparison is conducted under the grid resolution of 10 m, leading to the grid system of 800×800 . The simulated profiles of water levels and velocities (u and v) on the diagonal line are drawn in Figs. 3a, 3b, and 3c. The analytical solutions are also plotted in these figures. Concerning the water level profiles (Fig. 3a displays), the results of the FV-HLLC and SWFCA models both match the analytical solutions well, but the WCA2D model can only produce a still water level profile. As to the u -velocity profiles (depicted in Fig. 3b), the results of the FV-HLLC and SWFCA models are both in good agreement with the analytical profile despite some overestimations nearby the moving wet-dry interfaces. From Fig. 3b, the SWFCA model has less overestimation on the u -velocity profile around the wet-dry interfaces than the FV-HLLC model. From the viewpoint of the v -velocity profiles (drawn in Fig. 3c), both the FV-HLLC and SWFCA models provide reliable and identical predictions. The L_2 norms for water levels and velocities are listed in Table 3 for comparison.

From Figs. 3a, 3b, and 3c and Table 3, the WCA2D model fails to simulate the flows in Case A because it lacks the consideration of inertias. The SWFCA model is confirmed to be as accurate as the FV-HLLC model on water level and v -velocity profiles and can be more accurate than the FV-HLLC model on u -velocity profiles, particularly around the wet-dry interfaces. This result is related to the differences in determining the water velocities between the two models. In the selected FV-HLLC model, the water velocity is indirectly calculated and inversely proportional to the water depth since the model solves conserved variables (d, du, dv), making the water velocity increase to a spurious extent at the

Table 3

The comparison of the numerical accuracy among the WCA2D, FV-HLLC, and SWFCA models in the six strong discontinuous flow cases.

Scenarios	(1) WCA2D L_2	(2) FV-HLLC L_2	(3) SWFCA L_2
Case A	water level 0.147	<0.001	<0.001
	u -velocity 1.000	0.016	0.005
	v -velocity 1.000	0.046	0.045
Case B	discharge at outlet 0.723	0.177	0.065
	discharge at hillside 0.640	0.047	0.045
Case C	depth 0.215	0.041	0.041
	velocity 0.244	0.048	0.048
Case D			
Dry bed condition with the open end	depth 0.643	0.236	0.236
Wet bed condition with the closed end	depth 0.609	0.190	0.190
Case E	maximum water level arrival time 0.098	0.080	0.080
	0.193	0.115	0.115
Case F			
Low inflow	depth 0.395	0.247	0.247
Medium inflow	depth 0.380	0.231	0.231
High inflow	depth 0.379	0.214	0.214

wet-dry interface where water depth is quite small (Toro, 2001). On the other hand, the SWFCA model decides the predicted water depth and then finds the predicted water velocity by a special form of the energy equation with friction loss (Eqs. (11), (13), or (14) in Step 4, and Eqs. (16) and (17) in Step 5) such that the water velocity at the wet-dry interface is constrained by the friction loss term. Thus, the SWFCA model produces less overestimation of the water velocity compared to

the FV-HLLC model.

3.2.2. Case B: Shallow overland flows in a steep V-shape catchment (moving wet-dry interfaces)

In Case B, very shallow overland flows and channel flows are involved in an idealized V-shape catchment (Xia et al., 2017; Hou et al., 2018; Zhao and Liang, 2022). This study case was originally studied by

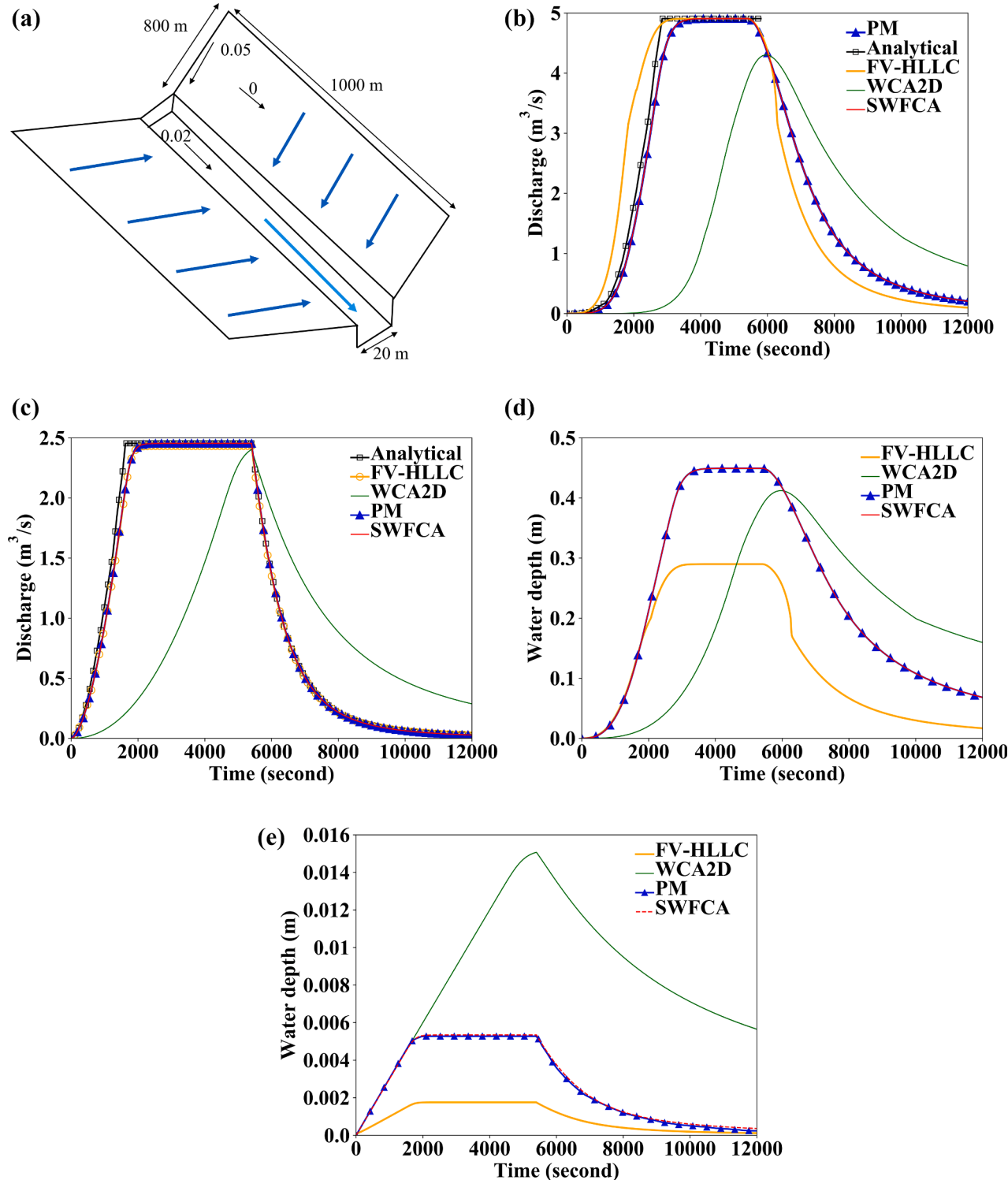


Fig. 4. Shallow overland flows in a steep V-shape catchment (Case B). (a) The geometry. The numerical comparison for the (b) discharge hydrographs at the channel outlet, (c) discharge hydrographs at the hillside, (d) time series of water depths at the channel outlet, and (e) time series of water depths at the downstream end of the hillside. The PM model refers to the FV-HLLC model by Zhao and Liang (2022).

Di Giacomo et al. (1996) and the analytical solutions for discharge hydrographs were provided by utilizing the kinematic wave theory. Later, Simons et al. (2014) reproduced the analytical solutions. The rectangular computational domain consists of two hillsides with the same size of 1000 m × 800 m and a 20 m wide 1000 m long channel in between the two hillsides, as illustrated in Fig. 4a. On the two hillsides, the slopes in the directions parallel and normal to the channel are 0 and 0.05, respectively. As to the channel, the slope is 0.02 and the depth of it ranges from 1 m (upstream end) to 20 m (downstream end). A uniform rainfall with a constant rainfall intensity of 10.8 mm/hr drops water on the two hillsides for 1.5 hrs. All boundaries are closed except for the channel outlet, where the open boundary condition (the same as the transmissive boundary condition) is imposed to let water flows out.

Initially, the whole computational domain is dry. The simulation duration is about 3.3 hrs (=12000 s). When the rainfall started, the water fell on the hillsides and became very shallow overland flows due to the steep slope. These runoffs then flowed into the channel with a sudden drop in terrain. After the rainfall stopped, the runoffs began to recede and the computational domain gradually dried. The Manning's roughness coefficients are $0.015 \text{ s/m}^{1/3}$ on the hillsides and $0.15 \text{ s/m}^{1/3}$ on the channel. To quantify the numerical accuracy, the simulated and analytical discharge hydrographs at the hillside and the channel outlet are used to determine two L_2 norms for discharge hydrographs. Hence, the computations of L_2 norms use 11,880 and 5,805 data at the hillside and the channel outlet, respectively. Similar to Case A, a grid convergence test is performed and the grid resolution of 10 m is recognized to be the most suitable. Therefore, for the following accuracy comparison, the square cell with the length of 10 m is used to discretize the computational domain into 16,463 cells.

Figures 4b and 4c depict the simulated discharge hydrographs at the channel outlet and hillside, respectively. The analytical solutions are also drawn in these figures. Obviously, the FV-HLLC model fails to simulate the discharge hydrograph at the channel outlet correctly. Thus, the simulated results of another FV-HLLC model with a more robust scheme (*i.e.*, the PM model by Zhao and Liang, 2022) are included in the figures as the PM model. Clearly, the SWFCA and PM models have very identical results that are both in close agreement with the analytical solutions. On the other hand, the FV-HLLC model can only provide satisfactory results for the discharge hydrograph at the hillside since it cannot resolve the partially wet condition in Case B (Zhao and Liang, 2022). The discharge hydrographs of the WCA2D model are both significantly delayed because the intercellular velocities on the hillsides are forced not to exceed critical velocities.

The time series of water depths at the channel outlet and the downstream end of the hillside are drawn in Figs. 4d and 4e, respectively. Similar relations among the four models are shown again. The SWFCA model computes almost the identical water depth series compared to the PM model. On the other hand, the FV-HLLC model underestimates the water depths at both two locations, which is also seen in the work of Zhao and Liang (2022). The major cause of this difference is due to the incapability of the FV-HLLC model in handling the partially wet conditions that occurred on the hillside in Case B (Xia et al., 2017; Zhao and Liang, 2022). The L_2 norms for discharge hydrographs at the hillside and channel outlet of the selected models for this case are listed in Table 3. Inspection of Table 3 confirms that the SWFCA model is as accurate as the FV-HLLC model in predicting the discharge at the hillside, and has better performance on the discharge at the channel outlet than the FV-HLLC model. As to the WCA2D model, it is not suitable to simulate Case B.

To sum up, Cases A and B prove that the SWFCA model has the same accuracy as the FV-HLLC model and has better performance than the WCA2D model. Nevertheless, in the aspect of moving wet-dry interfaces (Case A) and flows under the partially wet condition (Case B), the SWFCA model is more robust than the selected FV-HLLC model and can even provide the same accurate results as another FV-HLLC model with more complicated numerical procedures (PM model by Zhao and Liang

(2022)) for Case B. This result is related to the numerical procedures in the SWFCA and FV-HLLC models. From the viewpoint of moving wet-dry interfaces in Case A, the water velocity and depth are inversely proportional in the selected FV-HLLC model such that the water velocity may raise to an extremely high value at the wet-dry interface because of the considerably small water depth. Conversely, the SWFCA model first updates the predicted water depth (Steps 2 and 3) and then computes the predicted water velocity (Step 4), letting the water velocity at the wet-dry interface be constrained by the friction loss term (Eqs. (11), (13) and (14)). In Case B, because the water depths on the hillsides (about 0.005 m from Fig. 4e) are much smaller than the bed elevation difference between two adjacent cells, the selected FV-HLLC model numerically defines the local Riemann problem as the dry-bed dam-break problem such that the uniform overland flows on the hillsides are modeled as waterfall, which is physically wrong (Xia et al., 2017). This "waterfall effect" can be resolved by using a more robust reconstruction method, like the PM model does (Zhao and Liang, 2022). Unlike the two FV-HLLC models, the SWFCA model directly uses nodal bed elevations to compute the transported mass and inertias, thus it can successfully handle this partially wet condition. Overall, the computing method of the SWFCA model has shown its capability to handle flows on uneven terrain and terrain with a steep hillside.

3.2.3. Case C: Transcritical river flows with hydraulic jump (transcritical flows)

Case C considers river flows with mixed flow conditions. The analytical solutions of the bed slope, bed elevation, and water depths provided by MacDonald et al. (1997) were all modified to fulfill the wide-rectangular channel assumption of the selected models. The length and width of the computational domain are 1000 m and 10 m, respectively. A time-invariant inflow of $20 \text{ m}^3/\text{s}$ is given on the left edge as the upstream boundary condition. As for the downstream boundary condition, a fixed water depth of 1.35 m from the exact water depth profile is set on the right edge to introduce the backwater effect.

Initially, the water depths of the computational domain are given as the exact water depths. As for the water velocities, they are initially given as zero. After the simulation starts, water comes from the upstream boundary and moves downward. To ensure the flows become steady again, the simulation lasts for 3600 s. The Manning's roughness coefficient of the computational domain is given as $0.02 \text{ s/m}^{1/3}$ (MacDonald et al., 1997). The simulated profiles of water depths and velocities at $t = 3600 \text{ s}$ are used to calculate the L_2 norms for water depths and velocities, respectively. To focus on the numerical performance around the hydraulic jump, only data with its x coordinate being between 550 m and 650 m is adopted for the computations of L_2 norms. After a grid convergence test like Case A, square cells with a cell length of 1 m are used to discretize the computational domain into 11,011 computational cells. Consequently, there are 101 uniformly distributed data used for determining each L_2 norm.

The simulated water level profiles of the three selected models are plotted in Fig. 5a. The analytical water level profile is displayed in Fig. 5a as well. As for the water velocity profiles, the simulated together with the analytical profiles are drawn in Fig. 5b. Apparently, from these two figures, the WCA2D model fails to correctly simulate the hydraulic jump as expected. Also, the WCA2D model cannot simulate supercritical flows because the water velocity is constrained by the critical flow equation. The simulated profiles of the SWFCA and FV-HLLC models are very similar and are both in good agreement with the analytical solution. The comparison of numerical accuracy is listed in Table 3. From this table and Figs. 5a and 5b, the SWFCA model has shown its ability to simulate hydraulic jump and it can provide the same accurate results as the FV-HLLC model.

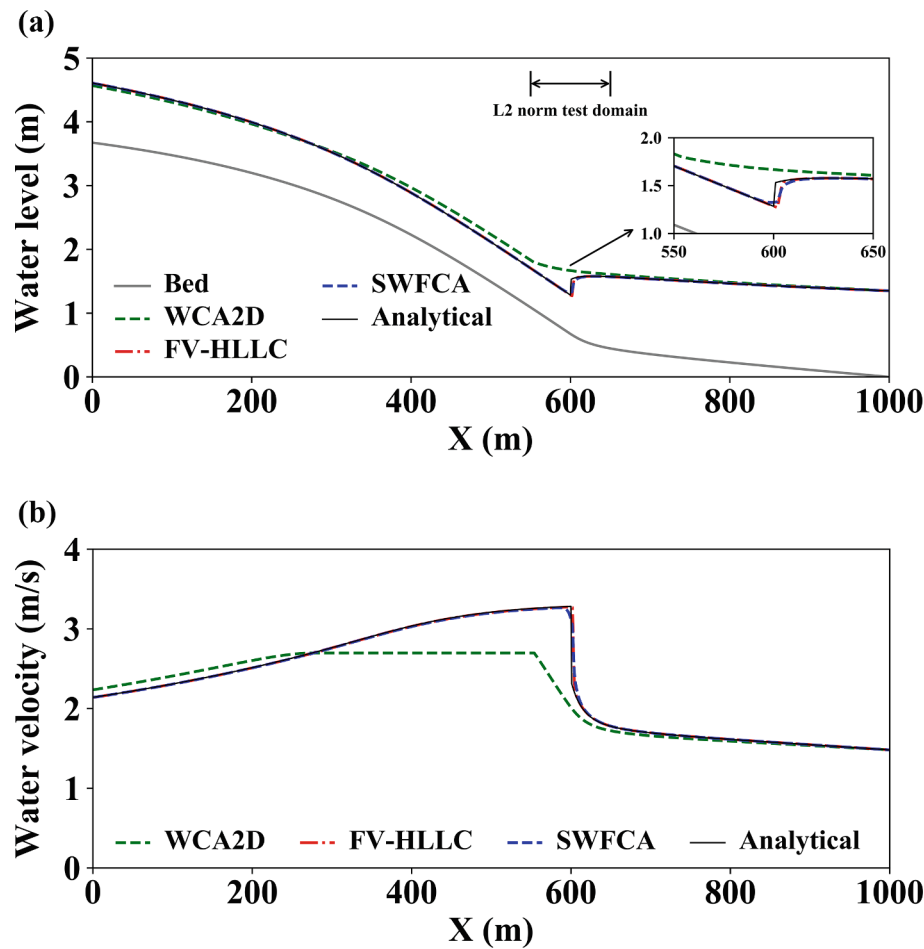


Fig. 5. Transcritical river flows with hydraulic jump (Case C): The comparison between the analytical solution and the numerical results of the (a) water levels and (b) velocities along the x direction.

3.2.4. Case D: dam-break flows over a symmetric triangular bump with various downstream boundary conditions (dam-break flows on idealized terrain)

In Case D, a CADAM test case (Morris, 2000) with moving dam-break flows over a symmetric triangular bump is studied (Zhou et al., 2004; Kao and Chang, 2012) to examine the performance of the proposed SWFCA model with complex boundary conditions. Partially reflective waves, hydraulic jumps/drops, and wet-dry interfaces all emerge because of the irregular bed slope. A reservoir with a length of 15.5 m, a width of 1.0 m, and a height of 1.0 m is connected to a rectangular rough channel with a length of 22.5 m. The gate of the reservoir is placed at $x = 15.5$ m. The center of the symmetric triangular bump is at $x = 28.5$ m with a length of 6.0 m and a height of 0.4 m. Both the slopes in the reservoir and the channel are zero. The configuration of the case is depicted in Fig. 6a. Water depth hydrographs were measured at four water depth gauges (*i.e.*, G4, G10, G13, and G20 as their locations are displayed in Fig. 6a). There were originally-three scenarios tested in the case.

The present study adopts the first two scenarios among the three scenarios because the WCA2D model cannot simulate the third scenario. The first scenario refers to the dry bed condition with the open end at the right edge, and the second scenario is the wet bed condition with the closed end at the right edge. In these two scenarios, the initial water depth in the reservoir is given as 0.75 m. As to the downstream boundary conditions, in the first scenario, the downstream channel located at the downstream side of the triangular bump is initially dry, and this channel is open at the right end, as Fig. 6a illustrates. For the second scenario, an initial water depth of 0.15 m is prescribed on the downstream channel

by incorporating a vertical wall at the end of the channel (drawn in Fig. 6b). In both two scenarios, dam-break flows propagate downward in the supercritical flow condition after the simulations start. The simulation durations of the two scenarios are both 40 s. The Manning's roughness coefficient is $0.0125 \text{ s/m}^{1/3}$ (Chang et al., 2011; Kao and Chang, 2012). Concerning the settings of the boundary conditions at the right end, the open and closed ends are respectively prescribed as the transmissive and reflective boundaries for both the SWFCA and FV-HLLC models. L_2 norms for water depths are used to evaluate the numerical accuracy of the three selected models. For each L_2 norm, the simulated water depth hydrographs at the four gauges are all used with the measured data to determine a single L_2 norm value. Thus, for each selected model, there are 142 and 152 data used for the computation of water depth L_2 norms in the first and second scenarios, respectively. A grid convergence is undertaken in the same way as Case A, and the computational domain is discretized by square cells with a length of 0.1 m, leading to 4,411 cells.

The simulated water depth hydrographs at the four selected gauges in the first and second scenarios are plotted in Figs. 6c and 6d, respectively. The simulated water level profiles of the three models at $t = 9.7$ s in the two scenarios are presented in Figs. 6e and 6f, respectively. The measured data is also displayed in these figures. From Figs. 6c and 6d, in both the two scenarios, there exist significant discrepancies between the simulated results of the WCA2D model and the measured data at these four water depth gauges. Specifically, the overtopping of water across the triangular bump and the reflective wave are both not correctly simulated by the WCA2D model. This result is majorly attributed to the use of the critical flow equation that constrains the water velocity of the

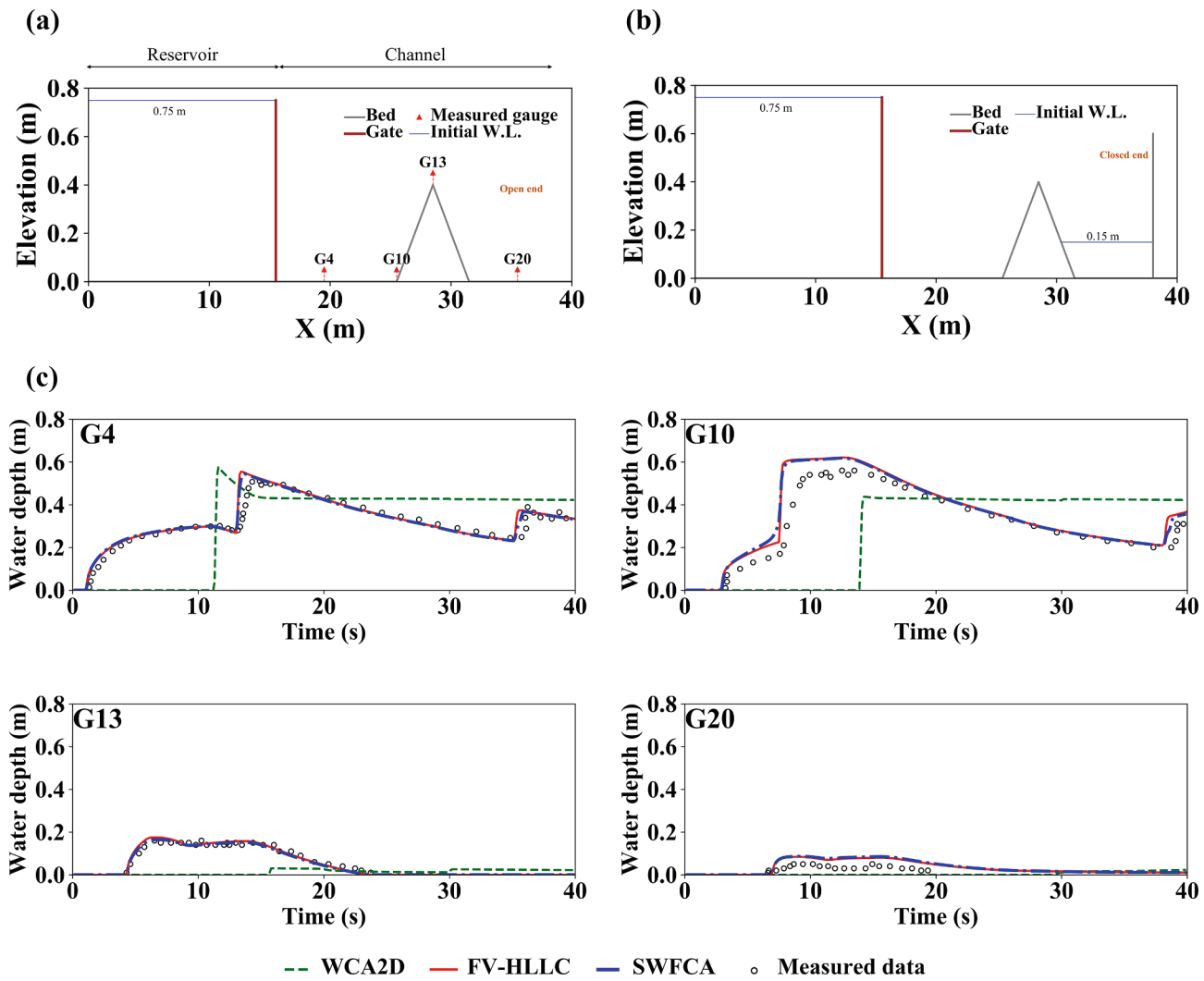


Fig. 6. Dam-break flows over a symmetric triangular bump with various downstream boundary conditions (Case D). Two scenarios are studied, i.e., the dry bed condition with the open end scenario (first scenario) and the wet bed condition with the closed end (second scenario). Layouts and settings of the (a) first and (b) second scenarios. The comparison between the simulated and experimental results of the water depths at the four measured gauges of the (c) first and (d) second scenarios. Simulated profiles of the water levels at $t = 9.7$ s of the (e) first and (f) second scenarios.

dam-break front. By contrast, the SWFCA and FV-HLLC models both provide accurate enough profiles in spite of some small discrepancies between the simulated profiles and measure data at water depth gauge G20. These differences are also observed in Chang et al. (2011) since the selected models are 2D shallow water flow models that lack the consideration of vertical acceleration terms in their numerical schemes. Nevertheless, inspection from Figs. 6e and 6f reveals that the SWFCA and FV-HLLC models provide almost identical water level profiles and both successfully simulate partially reflective waves as well as hydraulic jumps/drops. On the other hand, the WCA2D model fails to give reasonable outcomes. The L_2 norms for water depths of the three models in the two scenarios are displayed in Table 3, which confirms that the accuracy between the SWFCA and FV-HLLC models is very identical. Hence, the computing method of the SWFCA model can successfully simulate very complicated flows with moving shock waves, partially reflective waves, and overtopping water amounts accurately in these two scenarios.

3.2.5. Case E: Malpasset dam-break event on the Reyran river floodplain (dam-break flows on realistic terrain)

The Malpasset dam-break event is a real dam-break event that

happened in France in 1959, killing 423 people in the resulting flood on the downstream side of the Reyran river floodplain. This dam-break event is included in the CADAM project (Soares-Frazão et al., 1999) and is a useful benchmark case for studying dam-break waves propagation in a natural topography (Kao and Chang, 2012; Hou et al., 2013). The configuration of the Reyran river floodplain is drawn in Fig. 7a for illustration. The local police investigated and reported the maximum water levels at 17 locations (P1 to P17) along the Reyran river valley (Soares-Frazão et al., 1999). Three electric transformers (T1 to T3) were destroyed by the flood and their shutdown times represent the wave arrival times of the flood wave. Moreover, a non-distorted 1:400 scale model was built and calibrated against the observations aforementioned. From this scale model, the maximum water levels and wave arrival times of 9 gauges (S6 to S14) downstream the dam were measured. The locations of the aforementioned 17 investigated points, 3 electric transformers, and 9 experimental gauges are depicted in Fig. 7a.

Initially, the whole computational domain is assumed to be dry except for the reservoir where a constant water level of 100 m with zero velocities is prescribed. The boundaries in the sea are opened and the rest boundaries are closed. The simulation lasts for 3600 s, and the Manning's roughness coefficient of the computational domain is given

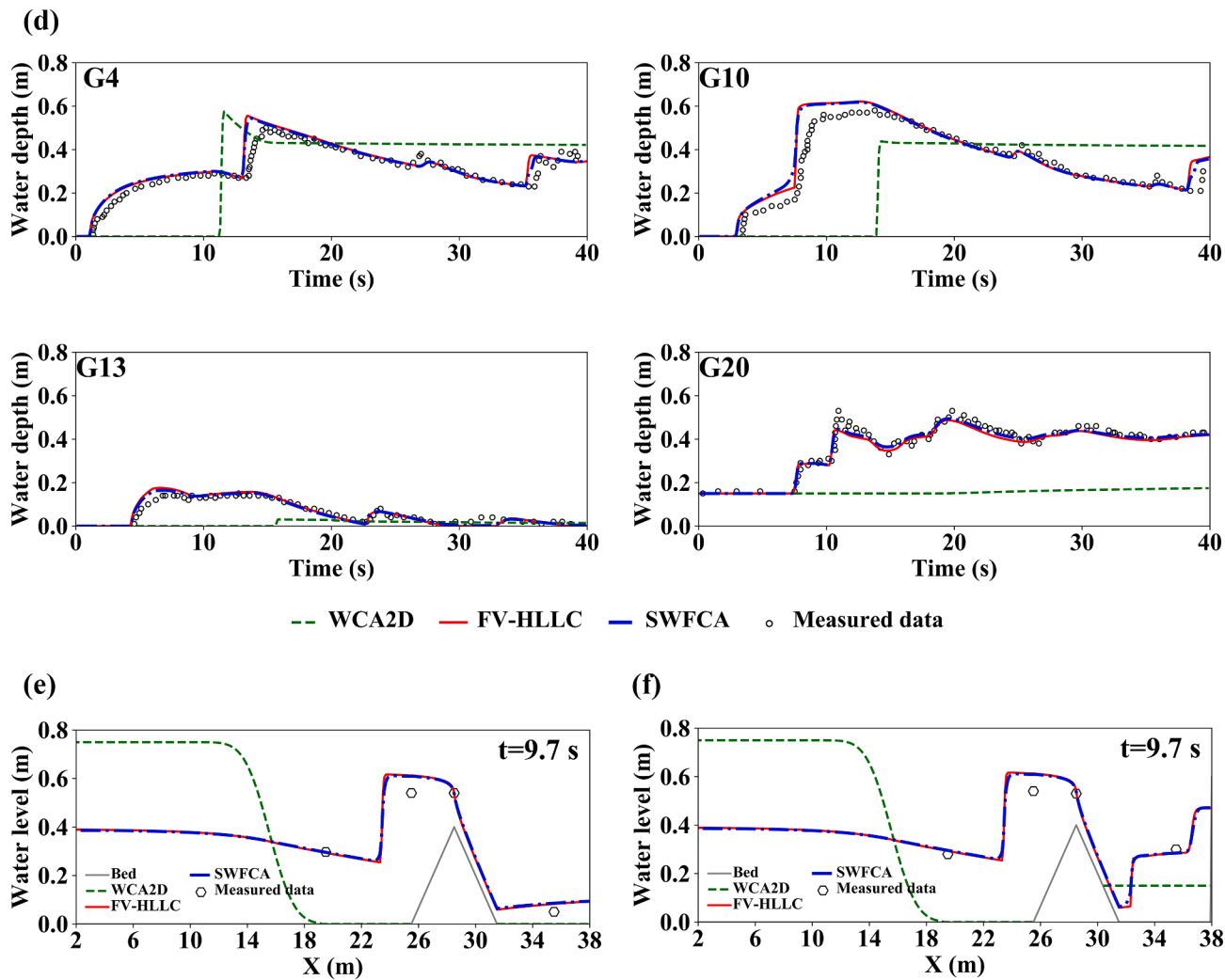


Fig. 6. (continued).

as $0.033 \text{ s/m}^{1/3}$ (Kao and Chang, 2012; Hou et al., 2013). The Malpasset dam is simplified as a straight line in the narrow valley of the Reyran river and the ruins of the dam are assumed to have no effects on the dam-break flows (Soares-Frazão et al., 1999). The maximum water levels at the 17 investigated points and 9 experimental gauges are used to calculate a single L_2 norm for the maximum water levels. Similarly, a single L_2 norm for wave arrival times is decided by using the arrival times at the 3 electric transformers and 9 experimental gauges. Similar to previous Cases, a grid convergence test is taken and the computational domain is subsequently discretized into 520,359 square cells with a length of 10 m. The bed elevation of each computational cell is interpolated by employing the natural neighbor interpolation.

Figures 7b and 7c display the simulated maximum water levels at the 17 investigated points and at the 9 experimental gauges, respectively. The wave arrival times at the 3 electric transformers and the 9 experimental gauges are drawn in Figs. 7d and 7e, respectively. The measured data is included in these figures for comparison. The simulated results of the SWFCA and FV-HLLC models are found to be very similar and agree reasonably well with the measured data. On the other hand, the WCA2D model tends to overestimate the maximum water levels in the narrow valley (*i.e.*, P3, P5, P6, P8, and S10) and underestimate the maximum water levels in the downstream floodplain (*i.e.*, P10 to P17 and S11 to S14). This result is related to the use of the critical flow equation in the WCA2D model that slows down the movement of the dam-break flows, leading to the underestimations of the arrival times (shown in Figs. 7d and 7e). The L_2 norms for the maximum water levels and arrival times

are listed in Table 3. As the L_2 norms between the SWFCA and FV-HLLC models are the same, the SWFCA model is found to have the same accuracy as the FV-HLLC model on simulating 2D dam-break flows in a realistic river floodplain.

3.2.6. Case F: Discharge flows over the Toce floodplain with staggered buildings (dam-break flows on realistic terrain)

In this case, dam-break flows towards buildings in the staggered configuration are studied by adopting the experimental case originating from IMPACT and CADAM projects (Testa et al., 2007). In the present study, the original valley geometry scaled 100 times down from the Toce river valley is adopted, as shown in Fig. 8a. All the three inflows hydrographs given at the left edge are adopted (displayed in Fig. 8a as well), leading to three scenarios in Case F as low, medium, and high inflow scenarios. In these three scenarios, a staggered building layout is considered (Fig. 8a). Ten water depth hydrographs were measured at ten water depth gauges (locations are also depicted in Fig. 8a).

The simulation durations of the three scenarios are all 60 s. The elevations of the cells where the buildings locate are raised up by 0.15 m. The Manning's roughness coefficient is given as $0.0162 \text{ s/m}^{1/3}$ as suggested by Testa et al. (2007). Among ten water depth gauges, the water depth hydrographs at eight gauges (P3 to P10 in Fig. 8a) are used to determine a single water depth L_2 norm (Yu and Chang, 2021). Consequently, there are 2,408 measured data for the computation of each L_2 norm for water depth. A grid convergence test is performed and square cells with a cell size of 2.5 cm are used to discretize the computational

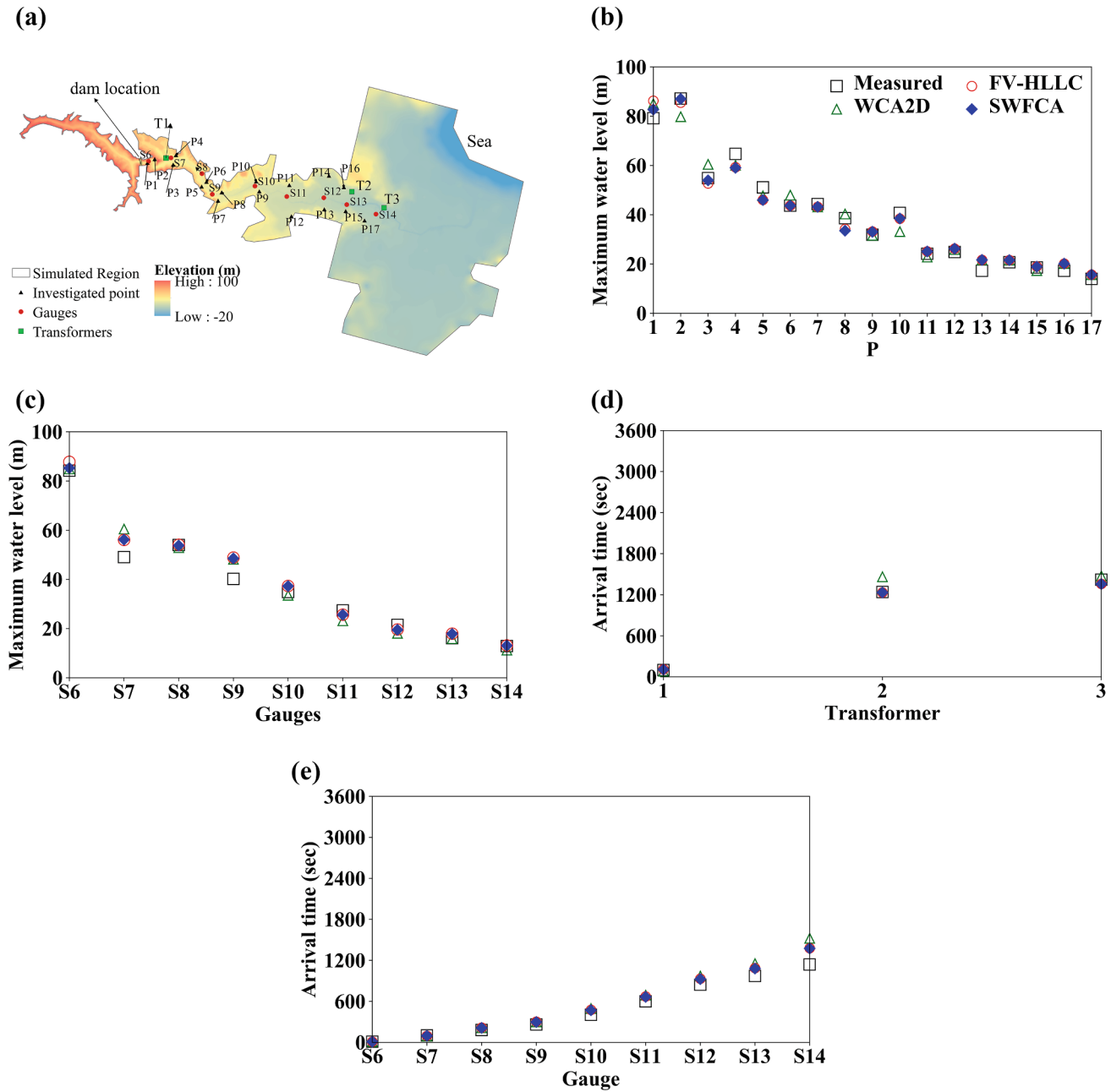


Fig. 7. Malpasset dam-break event on the Reyran river floodplain (Case E). (a) The configuration of the Reyran river floodplain and the positions of the 17 investigated points (P1 to P17), 3 electric transformers (T1 to T3), and 9 experimental gauges (S6 to S14). The comparison between the simulated and measured results of the (b) maximum water levels at the 17 investigated points, (c) maximum water levels at the 9 experimental gauges, (d) arrival times at the 3 electric transformers, and (e) arrival times at the 9 experimental gauges.

domain into 54,964 cells.

Figs. 8b, 8c, and 8d display the simulated and measured profiles of water depths at the selected gauges for the low, medium, and high inflow scenarios, respectively. From these figures, the simulated results of the SWFCA and FV-HLLC models all match the measured data reasonably well at the selected gauges. Nonetheless, for the WCA2D model, the simulated water depths at the P3 to P6 gauges are obviously underpredicted. This result is because the WCA2D model cannot reflect the raise of water depths due to hydraulic jumps (Costabile et al., 2017). Nevertheless, at the P7 to P10 gauges, the WCA2D model is capable to give satisfactory water depths because the flow conditions turn into regular flows. The L₂ norms for water depths in the three scenarios are calculated and listed in Table 3 for accuracy comparison. In Table 3, the accuracy of the SWFCA model is again demonstrated to be the same as

the FV-HLLC model. Hence, it is confirmed that the proposed SWFCA model has the ability to accurately simulate 2D dam-break flows on a complex terrain with hydraulic jumps/drops and moving wet-dry interfaces in Case F.

Based on the results from Cases D, E and F, the SWFCA model has shown its remarkable robustness on handling the complex interactions between dam-break flows, topography, and boundary conditions. Through the accuracy comparison between the simulated and analytical results, the SWFCA model can achieve good accuracy as the FV-HLLC model on partially reflective waves, hydraulic jumps/drops, moving wet-dry interfaces, and regular flows on idealized and realistic terrain. Hence, the SWFCA model can produce reliable results on dam-break flows. The WCA2D model has less accuracy than the SWFCA model as expected.

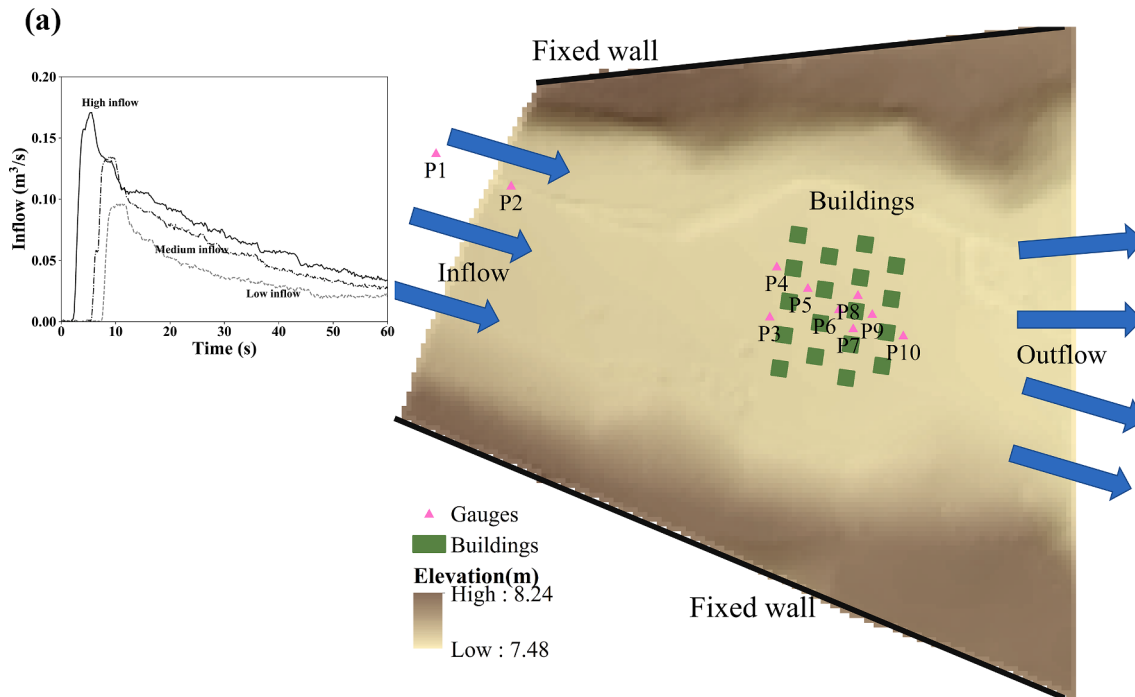


Fig. 8. Discharge flows over the Toce river floodplain with staggered buildings (Case F). (a) Layout and three inflow hydrographs of this case. The comparison between the simulated and experimental results of the water depths at eight gauges in the (b) low, (c) medium, and (d) high inflow scenarios.

In general, the SWFCA model can accurately simulate regular flows and strong discontinuous flows through these representative cases. The WCA2D model is found to have satisfactory accuracy only in cases with a small portion of strong discontinuous flows. On the other hand, the SWFCA model is as accurate as the FV-HLLC model in these selected cases, which is not surprising because the used form of the energy equation in the SWFCA model is actually another special form of the 2D SWEs. Also, the L_2 norms for evaluating the numerical accuracy use a relatively large range of simulated/measured data. Nevertheless, the SWFCA model has better accuracy than the FV-HLLC model for simulating moving wet-dry interfaces and flows under the partially wet condition. Despite that, it is still worth mentioning that the performance of the SWFCA model in other cases with stronger discontinuities should be tested in the future.

4. Model efficiency assessment

Section 3 has demonstrated through ten cases that the SWFCA model can accurately simulate regular flows and strong discontinuous flows. In particular, for strong discontinuous flows, the SWFCA model is as accurate as the FV-HLLC model and can be more accurate than the FV-HLLC model under specified flow conditions. On the other hand, the WCA2D model can only provide satisfactory results on regular flows. The next issue is about the efficiency of the SWFCA model. In this section, the model efficiency of the SWFCA model is assessed and compared with the WCA2D model through the ten cases in Section 3. In total, there are thirteen simulations for each model. To minimize the differences in the numerical implementation, the SWFCA model is written in the same code structure as the WCA2D model, and their simulations are all executed on an Intel (R) Core (TM) i9-9900K PC equipped with 6.0 GB RAM without activating parallel computing. The clock speed of the core is 3.4 GHz.

The total CPU time of the two models in the ten cases is recorded and listed in Table 4. In terms of the regular flow cases, the WCA2D model takes more the total CPU time than the SWFCA model in the first and third cases, mainly because the moving wet-dry fronts of the inflows

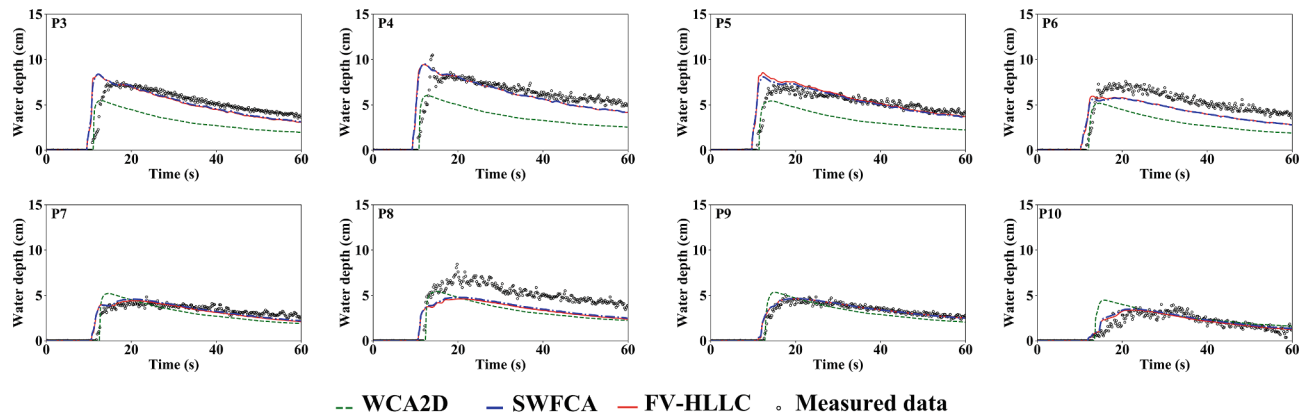
occurred in these two cases involve considerably high Froude numbers. By contrast, the WCA2D model outperforms the SWFCA model in the second and fourth cases as expected. For the strong discontinuous flow cases, in Case A, the WCA2D model spends less the total CPU time than the SWFCA model simply because there is no intercellular-volume computation after the simulated water levels become still. From the other five cases, the SWFCA model is 162.9 % to 23760.0 % faster than the WCA2D model since the latter tend to use very small adaptive time steps to stably propagate flows. This result may also be attributed to the fact that the grid resolutions in Cases B to F are quite small, making the adaptive time steps of the WCA2D model very small to comply with the required accuracy. Conversely, the SWFCA model can efficiently simulate regular flows and strong discontinuous flows.

Nevertheless, because the involved flow conditions in these ten cases are quite different, it is difficult to explain the above results by the deduction in Section 2.4. Thus, an extended evaluation to investigate the model efficiency of the SWFCA model in a designed condition is conducted next.

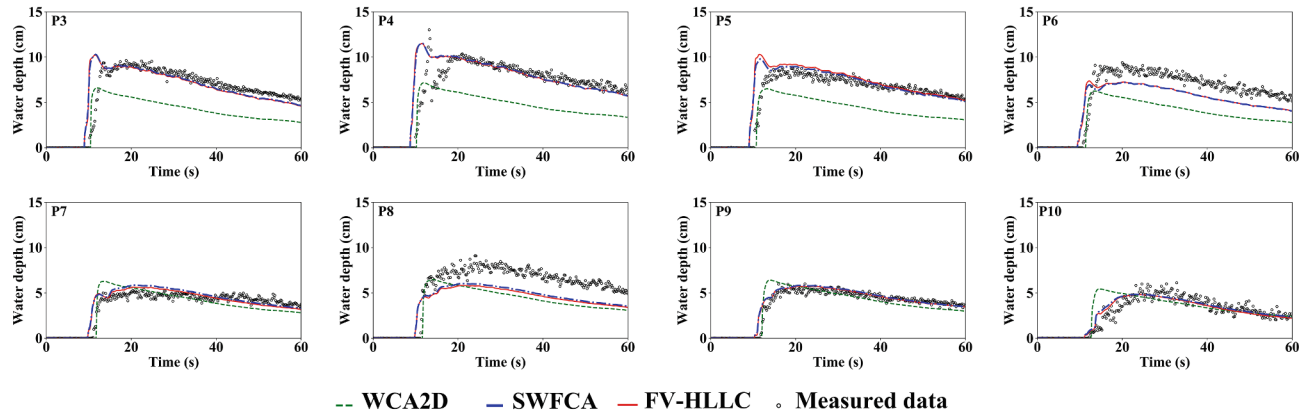
5. Extended model efficiency evaluation

As discussed in Section 2.4, the total CPU time is influenced by the required time to execute the solving procedure in each time step and the magnitudes of adaptive time steps. Consequently, the flow conditions involved also have an impact on the efficiency of the WCA2D and SWFCA models. When the portion of strong discontinuous flows in the computational domain increases, the SWFCA model could simulate more efficiently than the WCA2D model. As the portion is small, the WCA2D model is faster than the SWFCA model. Despite the efficiency comparison of the SWFCA and WCA2D models is performed in Section 4, it is very hard to explain the compared results as the flow conditions in ten cases are different. Therefore, an extended model efficiency evaluation with various designed flow conditions is conducted to qualitatively compare the efficiency between the WCA2D and SWFCA models. The FV-HLLC model used in Section 3 is included for efficiency comparison as well and it's also rewritten in the same code structure as the WCA2D

(b)



(c)



(d)

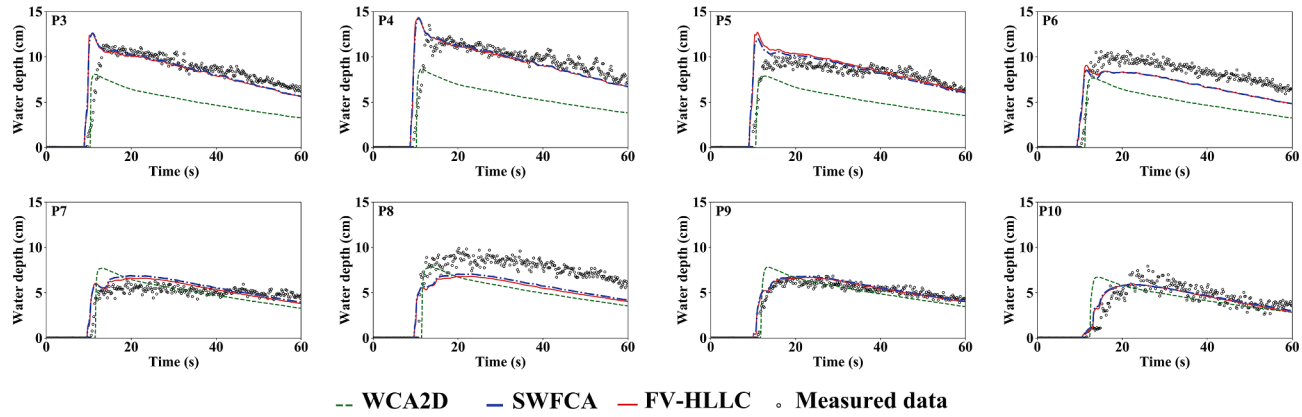


Fig. 8. (continued).

model for the comparison.

For non-inertia wave numerical models, to maintain physical and numerical stabilities, the adaptive time steps are quadratically decreased with respect to grid resolutions, which subsequently introduces heavy computational loads (*i.e.*, very long the total CPU time) for fine grid resolutions (Hunter et al., 2005). Generally, non-inertia wave models are often used on problems with relatively coarser grids (Caviedes-Voullième et al., 2020). This characteristic also accounts for the significant difference of efficiency between the WCA2D and SWFCA models in strong discontinuous flow cases. Thus, to have a fair comparison, this extended model efficiency evaluation uses the same layout

of Case F but scales it back to the original scale. In this way the cell length of each computational cell is 2.5 m. A short-duration (130 mins) heavy rainfall event that occurred on 21 August 2019 in Taipei City is used (20190821 flood event, see Fig. 5a in Chang et al. (2021)). The details of this event have been listed in Table 1 of Chang et al. (2021). The Manning's roughness coefficient is given as $0.025 \text{ s/m}^{1/3}$. In this extended evaluation, the bed slope of the computational domain is decreased by five factors (1, 1/2, 1/4, 1/8, and 1/16) to slow down water velocities, leading to five scenarios (100.0 %, 50.0 %, 25.0 %, 12.5 %, and 6.3 % bed slopes) with various flow conditions, and the portion of strong discontinuous flows is expected to reduce as the bed

Table 4

The efficiency comparison between the WCA2D and SWFCA models in the ten test cases of the model verification.

Cases	Scenarios	(1) WCA2D	(2) SWFCA	(3) The ratio of the total CPU time between the WCA2D and SWFCA models (3)=(1)/(2) (%)
		The total CPU time (s)	The total CPU time (s)	(3)=(1)/(2) (%)
Regular flow cases				
Non-breaking wave	–	1198.9	20.4	5877.0 %
EAT2	–	14.0	32.8	42.7 %
EAT4	–	923.2	366.8	251.7 %
EAT8a	–	907.3	958.9	94.6 %
Strong discontinuous flow cases				
Case A	–	704.7	1138.0	61.9 %
Case B	–	5.7	3.5	162.9 %
Case C	–	1219.1	6.0	20318.3 %
Case D	Dry bed condition with the open end	436.7	1.9	22984.2 %
	Wet bed condition with the closed end	475.2	2.0	23760.0 %
Case E	–	16667.2	1361.3	1224.4 %
Case F	Low inflow	2385.9	51.2	4660.0 %
	Medium inflow	4275.6	74.1	5770.0 %
	High inflow	6696.0	110.2	6076.2 %

slope of the computational domain is decreased. The simulation durations of the five scenarios are determined as the times when the outflow is less than 5 % of the peak outflow. The accuracy requirement of the WCA2D model is the same as in Case F, i.e., the maximum difference in water depth between the simulated/measured is less than 0.1 m. All the simulations are executed on the same computer used in [Section 4](#).

The comparison of numerical efficiency is displayed in [Table 5](#), which shows that the SWFCA and FV-HLLC models are both faster than the WCA2D model when the bed slope of the computational domain is relatively steeper. As the bed slope of the computational domain is relatively milder, the WCA2D model outperforms the SWFCA and FV-HLLC models. The SWFCA model can be up to 305.5 % more efficient than the WCA2D model. As for the SWFCA and FV-HLLC models, the SWFCA model is about 121.0 %–128.2 % faster than the FV-HLLC model. The average time steps of the three models are all increasing as the bed slope of the computational domain is decreasing. The average time step of the WCA2D model is found to be much less than the SWFCA model in the steepest bed slope (100.0 % bed slopes scenario) and gradually becomes larger than the SWFCA model as the bed slope of the computational domain becomes milder. This result proves the deduction that the WCA2D model may not be advantageous if a relatively large part of the flow conditions in a simulation is severe flow conditions. The average time steps of the FV-HLLC model are all slightly larger than the SWFCA model because the SWFCA model indirectly simulates the local inertias of 2D SWES in its transition rules. Thus, the SWFCA model requires relatively smaller adaptive time steps by using relatively smaller CFL numbers to simulate local inertias compared to the FV-HLLC model. Nevertheless, the differences in the average adaptive time steps between the SWFCA and FV-HLLC models are small. Hence, it is reasonable that the numerical efficiency of the SWFCA model is higher than the FV-HLLC model since the latter introduces a longer the required time to execute its solving procedure in each time step ([Yu and Chang, 2021](#)). The portions of strong discontinuous flows in the five scenarios are displayed in [Fig. 9](#), and the average portions of strong discontinuous flows in these scenarios are 21.1 %, 18.8 %, 16.5 %, 11.5 %, and 7.0 %,

Table 5

The comparison of the numerical efficiency among the WCA2D, FV-HLLC, and SWFCA models on the extended model efficiency evaluation.

Bed slopes	WCA2D		FV-HLLC		SWFCA	
	(1)	(2)	(3)	(4)	(5)	(6)
100.0 %	498.8	0.054	209.4	0.184	163.3	0.162
50.0 %	322.7	0.087	154.7	0.246	123.5	0.220
25.0 %	136.6	0.210	114.9	0.322	93.0	0.295
12.5 %	57.2	0.517	91.4	0.402	75.2	0.380
6.3 %	49.3	0.724	87.0	0.460	71.9	0.439
Efficiency						
	The ratio of the total CPU time between the WCA2D and SWFCA models (%)	The ratio of the average time steps between the WCA2D and SWFCA models (%)	The ratio of the total CPU time between the FV-HLLC and SWFCA models (%)	The ratio of the average time steps between the FV-HLLC and SWFCA models (%)	The ratio of the total CPU time between the SWFCA and FV-HLLC models (%)	The ratio of the average time steps between the SWFCA and FV-HLLC models (%)
	(7)= $\frac{(1)}{(5)}$	(8)= $\frac{(2)}{(6)}$	(9)= $\frac{(3)}{(5)}$	(10)= $\frac{(4)}{(6)}$		
100.0%	305.5%	33.3%	128.2%	113.6%		
50.0%	261.3%	39.5%	125.3%	111.8%		
25.0%	146.9%	71.2%	123.6%	109.2%		
12.5%	76.1%	136.1%	121.5%	105.8%		
6.3%	68.6%	164.9%	121.0%	104.8%		

respectively. From [Fig. 9](#), it is confirmed that as the bed slope of the computational domain is decreased, water velocities are slowed down, and consequently the portion of strong discontinuous flows is decreased. Inspection of [Table 5](#) also proves that the numerical efficiency of the SWFCA and FV-HLLC models is related to the portion of strong discontinuous flows, and the numerical efficiency of the SWFCA and FV-HLLC models is higher than the WCA2D model as the portion of strong discontinuous flows is relatively larger (at most up to 305.5 %). When the portion of strong discontinuous flows is relatively smaller, the WCA2D model is again faster than the SWFCA and FV-HLLC models. In addition, the efficiency of the SWFCA model is found to be higher than the FV-HLLC model (121.0 %–128.2 %). Therefore, the SWFCA model is demonstrated to be more efficient than the WCA2D and FV-HLLC models.

6. Conclusions

This study proposes a new CA-based shallow water flow solver (SWFCA) that adopts the Bernoulli hydraulic head instead of water level as the key factor to distribute water movement directions. A novel methodology sequentially determining flow directions, mass fluxes, and inertias fluxes between two adjacent cells is established to link water depths and velocities. Four regular flow cases and six benchmark cases with strong discontinuous flows are selected to verify the numerical accuracy and efficiency of the SWFCA model with the WCA2D and FV-HLLC models. Then, the efficiency of the SWFCA model on various flow conditions is evaluated through an extended case with various portions of strong discontinuous flows. The analysis shows that the SWFCA and WCA2D models both provide satisfactory results on regular flows. In modeling strong discontinuous flows, the SWFCA model produces the same accurate results as the FV-HLLC model. Nevertheless, the SWFCA model has higher accuracy than the FV-HLLC model in simulating moving wet-dry interfaces and flows under the partially wet

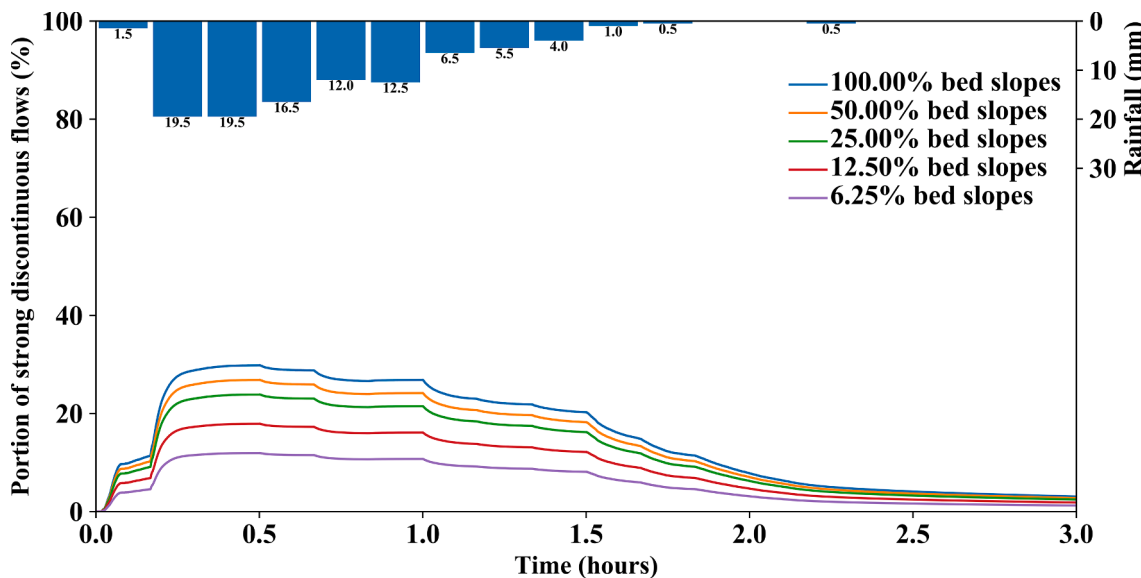


Fig. 9. The portion of strong discontinuous flows in the computational domain of the five scenarios in the extended model efficiency evaluation. The end time of each series in this figure is extended to 3 hrs to completely display the receding of the portion.

condition. As to the numerical efficiency, based on the outcomes from the extended case, the efficiency is confirmed to be related to the portion of strong discontinuous flows. When the portion of strong discontinuous flows is relatively large, the SWFCA model outperforms the WCA2D and FV-HLLC models by 305.5% and 121.0–128.2%, respectively. Hence, the SWFCA model can efficiently produce reliable 2D shallow water flow modeling results, which could be applied to real-time flood inundation modeling.

CRediT authorship contribution statement

Tsang-Jung Chang: Conceptualization, Methodology, Validation, Supervision, Project administration, Writing - review & editing. **Hsiang-Lin Yu:** Conceptualization, Methodology, Software, Validation, Formal analysis, Investigation, Data curation, Visualization, Writing - original draft, Writing - review & editing.

Declaration of Competing Interest

The authors declare that they have no known competing financial interests or personal relationships that could have appeared to influence the work reported in this paper.

Data availability

Data will be made available on request.

Acknowledgements

The accomplishment of this work is partially supported by the Ministry of Science and Technology, Taiwan, under Grant Nos. 109-2221-E-002-010-MY3. The authors are grateful for the support.

References

- Bates, P.D., Horritt, M.S., Fewtrell, T.J., 2010. A simple inertial formulation of the shallow water equations for efficient two-dimensional flood inundation modelling. *J. Hydrol.* 387 (1-2), 33–45.
- Cai, X., Li, Y., Wen Guo, X., Wu, W., 2014. Mathematical model for flood routing based on cellular automation. *Water Sci. Eng.* 7, 133–142.
- Castro-Orgaz, O., Hager, W.H. (Eds.), 2019. Shallow Water Hydraulics. Springer International Publishing, Cham.
- Caviedes-Voullième, D., Fernández-Pato, J., Hinz, C., 2018. Cellular automata and finite volume solvers converge for 2D shallow flow modelling for hydrological modelling. *J. Hydrol.* 563, 411–417.
- Caviedes-Voullième, D., Fernández-Pato, J., Hinz, C., 2020. Performance assessment of 2D Zero-Inertia and Shallow Water models for simulating rainfall-runoff processes. *J. Hydrol.* 584 (124663), 1–20.
- Chang, T.J., Kao, H.M., Chang, K.H., Hsu, M.H., 2011. Numerical simulation of shallow-water dam break flows in open channels using smoothed particle hydrodynamics. *J. Hydrol.* 408, 78–90.
- Chang, T.J., Chang, K.H., Kao, H.M., 2014. A new approach to model weakly nonhydrostatic shallow water flows in open channels with smoothed particle hydrodynamics. *J. Hydrol.* 519, 1010–1019.
- Cea, L., Bladé, E., 2015. A simple and efficient unstructured finite volume scheme for solving the shallow water equations in overland flow applications. *Water Resour. Res.* 51, 5464–5486.
- Chang, T.J., Chang, Y.S., Chang, K.H., 2016. Modeling rainfall-runoff processes using smoothed particle hydrodynamics with mass-varied particles. *J. Hydrol.* 543, 749–758.
- Chang, T.J., Yu, H.L., Wang, C.H., Chen, A.S., 2021. Overland-gully-sewer (2D-1D-1D) urban inundation modeling based on cellular automata framework. *J. Hydrol.* 603 (127001), 1–16.
- Chaudhry, M.H., 2022. Open-Channel Flow, Third Edition. Springer, U.S.
- Chopard, B., 2009. Cellular automata modeling of physical systems. *Encyclopedia of Complexity and Systems Science*, Springer, New York, pp. 856–892.
- Costabile, P., Costanzo, C., Macchione, F., 2017. Performances and limitations of the diffusive approximation of the 2-d shallow water equations for flood simulation in urban and rural areas. *Appl. Numer. Math.* 116, 141–156.
- Delestre, O., Cordier, S., Darboux, F., James, F., 2012. A limitation of the hydrostatic reconstruction technique for Shallow Water equations. *C. R. Math.* 350, 677–681.
- Di Giacomo, P., Todini, E., Lamberti, P., 1996. A conservative finite elements approach to overland flow: the control volume finite element formulation. *J. Hydrol.* 175, 267–297.
- Dottori, F., Todini, E., 2011. Developments of a flood inundation model based on the cellular automata approach: testing different methods to improve model performance. *Phys. Chem. Earth Parts ABC* 36, 266–280.
- Ghimire, B., Chen, A.S., Guidolin, M., Keedwell, E.C., Djordjević, S., Savić, D.A., 2013. Formulation of a fast 2D urban pluvial flood model using a cellular automata approach. *J. Hydroinformatics* 15, 676.
- Guidolin, M., Chen, A.S., Ghimire, B., Keedwell, E.C., Djordjević, S., Savić, D.A., 2016. A weighted cellular automata 2D inundation model for rapid flood analysis. *Environ. Modell. Softw.* 84, 378–394.
- Hou, J., Liang, Q., Simons, F., Hinkelmann, R., 2013. A 2D well-balanced shallow flow model for unstructured grids with novel slope source term treatment. *Adv. Water Resour.* 52, 107–131.
- Hou, J., Wang, T., Li, P., Li, Z., Zhang, X., Zhao, J., Hinkelmann, R., 2018. An implicit friction source term treatment for overland flow simulation using shallow water flow model. *J. Hydrol.* 564, 357–366.
- Hunter, N.M., Horritt, M.S., Bates, P.D., Wilson, M.D., Werner, M.G.F., 2005. An adaptive time step solution for raster-based storage cell modelling of floodplain inundation. *Adv. Water Resour.* 28, 975–991.
- Jahanbazi, M., Özgen, I., Aleixo, R., Hinkelmann, R., 2017. Development of a diffusive wave shallow water model with a novel stability condition and other new features. *J. Hydroinformatics* 19, 405–425.

- Jamali, B., Bach, P.M., Cunningham, L., Deletic, A., 2019. A cellular automata fast flood evaluation (CA-ffé) model. *Water Resour. Res.* 55, 4936–4953.
- Kao, H.M., Chang, T.J., 2012. Numerical modeling of dambreak-induced flood and inundation using smoothed particle hydrodynamics. *J. Hydrol.* 448–449, 232–244.
- Liu, L., Liu, Y., Wang, X., Yu, D., Liu, K., Huang, H., Hu, G., 2015. Developing an effective 2-d urban flood inundation model for city emergency management based on cellular automata. *Natural Hazards Earth Syst. Sci.* 15, 381–391.
- MacDonald, I., Baines, M.J., Nichols, N.K., Samuels, P.G., 1997. Analytical solutions for open-channel flows. *ASCE J. Hydraul Eng.* 123, 1041–1045.
- Milašinović, M., Randelović, A., Jaćimović, N., Prodanović, D., 2019. Coupled groundwater hydrodynamic and pollution transport modelling using Cellular Automata approach. *J. Hydrol.* 576, 652–666.
- Morris, M., 2000. CADAM: concerted action on dambreak modeling-final report. Rep. SR 571. HR Wallingford.
- S. Néelis G. Pender Benchmarking the lastest generation of 2D hydraulic modelling packages Environment Agency, Horison House, Deanery Road 2013 Bristol.
- Sampson, J., Easton, A., Singh, M., 2006. Moving boundary shallow water flow above parabolic bottom topography. *ANZIAM J.* 47, 373.
- P. Sarkhosh Y.C. Jin MPS-based model to solve one-dimensional shallow water equations *Water Resources Research* 57 2021 e2020WR028742.
- Simons, F., Busse, T., Hou, J., Özgen, I., Hinkelmann, R., 2014. A model for overland flow and associated processes within the Hydroinformatics Modelling System. *J. Hydroinf.* 16, 375–391.
- S. Soares-Frazão F. Alcrudo N. Goutal Dam-break test cases summary 1999 Zaragoza, Spain.
- Testa, G., Zuccala, D., Alcrudo, F., Mulet, J., Soares-Frazão, S., 2007. Flash flood flow experiment in a simplified urban district. *J. Hydraul. Res.* 45, 37–44.
- Toro, E.F., 2001. Shock-Capturing Methods for Free-Surface Shallow Flows. John Wiley, New York.
- Wang, Y., Chen, A.S., Fu, G., Djordjević, S., Zhang, C., Savić, D.A., 2018. An integrated framework for high-resolution urban flood modelling considering multiple information sources and urban features. *Environ. Modell. Software* 107, 85–95.
- Wolfram, S., 1984. Cellular automata as models of complexity. *Nature* 311, 419–424.
- Xia, X., Liang, Q., Ming, X., Hou, J., 2017. An efficient and stable hydrodynamic model with novel source term discretization schemes for overland flow and flood simulations. *Water Resour. Res.* 53, 3730–3759.
- Yin, D., Evans, B., Wang, Q., Chen, Z., Jia, H., Chen, A.S., Fu, G., Ahmad, S., Leng, L., 2020. Integrated 1D and 2D model for better assessing runoff quantity control of low impact development facilities on community scale. *Sci. Total Environ.* 720, 137630.
- Yu, H.L., Chang, T.J., 2021. A hybrid shallow water solver for overland flow modelling in rural and urban areas. *J. Hydrol.* 598 (126262), 1–17.
- Zhao, J., Liang, Q., 2022. Novel variable reconstruction and friction term discretization schemes for hydrodynamic modelling of overland flow and surface water flooding. *Adv. Water Resour.* 163, 104187.
- Zhou, J.G., Causon, D.M., Mingham, C.G., Ingram, D.M., 2004. Numerical prediction of dam-break flows in general geometries with complex bed topography. *J. Hydraul. Eng. ASCE* 130, 332–340.